

**FROUDE NUMBER AND SCALE EFFECTS AND FROUDE
NUMBER 0.35 WAVE ELEVATIONS AND MEAN-VELOCITY
MEASUREMENTS FOR BOW AND SHOULDER WAVE
BREAKING OF SURFACE COMBATANT DTMB 5415**

by

**A. Olivieri, F. Pistani, R. Wilson, L. Benedetti,
F. La Gala, E.F. Campana and F. Stern.**



IIHR Report No. 441

IIHR—Hydroscience & Engineering
College of Engineering
The University of Iowa
Iowa City, Iowa 52242-1585 USA

December 2004

Report Documentation Page				Form Approved OMB No. 0704-0188	
Public reporting burden for the collection of information is estimated to average 1 hour per response, including the time for reviewing instructions, searching existing data sources, gathering and maintaining the data needed, and completing and reviewing the collection of information. Send comments regarding this burden estimate or any other aspect of this collection of information, including suggestions for reducing this burden, to Washington Headquarters Services, Directorate for Information Operations and Reports, 1215 Jefferson Davis Highway, Suite 1204, Arlington VA 22202-4302. Respondents should be aware that notwithstanding any other provision of law, no person shall be subject to a penalty for failing to comply with a collection of information if it does not display a currently valid OMB control number.					
1. REPORT DATE DEC 2004		2. REPORT TYPE		3. DATES COVERED 00-00-2004 to 00-00-2004	
4. TITLE AND SUBTITLE Froude Number and Scale Effects and Froude Number 0.35 Wave Elevations and Mean-Velocity Measurements for Bow and Shoulder Wave Breaking of Surface Combatant DTMB 5415				5a. CONTRACT NUMBER	
				5b. GRANT NUMBER	
				5c. PROGRAM ELEMENT NUMBER	
6. AUTHOR(S)				5d. PROJECT NUMBER	
				5e. TASK NUMBER	
				5f. WORK UNIT NUMBER	
7. PERFORMING ORGANIZATION NAME(S) AND ADDRESS(ES) University of Iowa, College of Engineering, Iowa City, IA, 52242-1585				8. PERFORMING ORGANIZATION REPORT NUMBER	
9. SPONSORING/MONITORING AGENCY NAME(S) AND ADDRESS(ES)				10. SPONSOR/MONITOR'S ACRONYM(S)	
				11. SPONSOR/MONITOR'S REPORT NUMBER(S)	
12. DISTRIBUTION/AVAILABILITY STATEMENT Approved for public release; distribution unlimited					
13. SUPPLEMENTARY NOTES					
14. ABSTRACT see report					
15. SUBJECT TERMS					
16. SECURITY CLASSIFICATION OF:			17. LIMITATION OF ABSTRACT Same as Report (SAR)	18. NUMBER OF PAGES 62	19a. NAME OF RESPONSIBLE PERSON
a. REPORT unclassified	b. ABSTRACT unclassified	c. THIS PAGE unclassified			

TABLE OF CONTENTS

ABSTRACT.....	I
ACKNOWLEDGEMENTS.....	I
LIST OF SYMBOLS	II
1. INTRODUCTION	1
2. TEST DESIGN	2
2.1. Facilities.....	3
2.2. Model Geometries	4
2.3. Conditions.....	4
3. MEASUREMENT SYSTEMS, PROCEDURES, LOCATIONS AND DRE.....	5
3.1. Photo Study.....	5
3.2. Wave Elevations	5
3.3. Mean Velocities	6
3.4. Data Reduction Equations	7
4. UNCERTAINTY ANALYSIS	9
4.1. Wave Elevations	9
4.1.1. Bias Limit.....	10
4.1.2. Precision Limit.....	11
4.2. Mean Velocities	11
5. FROUDE NUMBER AND SCALE EFFECTS	11
5.1. Surface Tension and Viscous Effects	14
6. FROUDE NUMBER 0.35 WAVE ELEVATIONS AND MEAN VELOCITIES	17
7. COMPLEMENTARY CFD OBSERVATIONS	20
7.1. Free-Surface Wave Field and Flow	20
7.2. Boundary Layer and Free-Surface Vortices	21
8. A 3D BREAKING DETECTION CRITERION	22
9. CONCLUSIONS AND FUTURE WORK	23
REFERENCES	25
TABLES	27
FIGURES.....	31

ABSTRACT

This study is a good demonstration on how complementary EFD and CFD can provide a powerful and advanced tool in analysing complex industrial flows. Results are presented from a cooperative study between INSEAN and IIHR about wave and flow field measurement about a surface combatant with focus on the 3D ship wave breaking. At $Fr=0.35$, free-surface near and far fields have been measured, as well as the velocity in some transversal planes under the bow and shoulder wave. CFD computations have also been used to complete and extend EFD data and to understand some particular features of the flow, such as location of vortices near the free-surface and scars.

ACKNOWLEDGEMENTS

The research at INSEAN and IIHR was sponsored by the Office of Naval Research under Grants NICOP: N00014-00-1-0344 and N00014-01-1-0073, respectively, under the administration of Dr. Patrick Purtell. The research at INSEAN was also partially sponsored by the Italian Ministry of Transportation and Navigation in the frame of Research Plan 2000-2002.

LIST OF SYMBOLS

Alphabetical Symbols

a	Wave amplitude
B	Bias error
C_p	Pressure coefficient
e_0	Voltage output related to the undisturbed water level
f_s^{NF}	Sampling rate for the near field probe
f_s^{FF}	Sampling rate for the far field probe
f_s^V	Sampling rate for velocity measurements
Fr	Froude number, $U_0 / \sqrt{g L_{PP}}$
g	Gravity acceleration
h	Wave elevation
K_K	Calibration coefficient
L_{PP}	Length between perpendicular
Re	Reynolds number, $U_0 L / \nu$
t_a^V	Acquisition time interval for velocity measurements
t_a^{NF}	Acquisition time interval for the near field probe
U_0	Carriage velocity
We	Weber number, $U_0 \sqrt{\rho L_{PP} / \sigma}$
We_λ	Wavelength based Weber number, $U_0 \sqrt{\rho \lambda / \sigma}$
x	Longitudinal axis
y	Transversal axis
z	Vertical axis
$\Delta x^{NF}, \Delta y^{NF}$	Transversal and longitudinal spacing for the grid adopted for the near field free-surface measurements
$\Delta x^{FF}, \Delta y^{FF}$	Transversal and longitudinal spacing for the grid adopted for the far field free-surface measurements
$\Delta x_g^V, \Delta z_g^V$	Transversal and vertical spacing for the grid adopted for the velocity measurements

Greek Symbols

α, ϕ	Measured pitch and yaw angles of a velocity vector in 5-hole Pitot probe coordinates
α_p, ϕ_p	5-hole Pitot probe preset pitch and yaw angles
λ	Wave length
ρ	Water density
σ	Surface tension
θ	Sensitivity coefficient in uncertainty assessment; and local wave steepness
ν	Kinematic viscosity

FROUDE NUMBER AND SCALE EFFECTS AND FROUDE NUMBER 0.35 WAVE ELEVATIONS AND MEAN-VELOCITY MEASUREMENTS FOR BOW AND SHOULDER WAVE BREAKING OF SURFACE COMBATANT DTMB 5415

1 INTRODUCTION

The motion of marine vehicles traveling at sea usually leads to the formation of steep diverging bow and stern waves, possibly breaking. Depending on speed and geometry, a sequel of interesting phenomena follows: the generation of vorticity in the breaking region, the appearance of free-surface scars, and the entrainment of air, to name a few.

The present report is aimed at illustrating an experimental campaign focused in providing detailed experimental data for the 3D wave breaking generated by a fast displacement ship model, the DTMB 5415, conceived by David Taylor Model Basin as a preliminary design for a surface combatant (ca. 1980) with a sonar dome bow and transom stern.

The experimental campaign was carried out in the framework of a long term international collaboration between INSEAN and IIHR (see also [1], [17]) focused in providing detailed experimental data for a fast displacement ship model.

The purpose of present investigation is to increase our knowledge of the flow field near an advancing surface ship when breaking waves are produced. This work also stems from the difficulty in modeling this complex flow and hence from the strong need of accurate and tailored experimental campaigns dedicated to collecting data for benchmarking.

As Duncan [6] points out, recent literature dedicated to the subject is concentrated to PIV measurements of the breakers in the bow waves of a ship model, e.g. Dong et al. [9] and Roth et al., [10]. In both these studies the focus is on the flow within the attached liquid sheet close to the stem of the ship model, to analyse the structure of the bow wave, and do not extend the investigation to the downstream evolution of the free-surface flow after the breaking, including wave induced vortices.

Analyzing the flow past a ship in drift condition, Longo and Stern [20] show the presence of a bow wave breaking induced vortex on the suction side of the model.

However, previous data collected for zero drift condition does not show bow wave breaking.

Here, a much more complete set of data is presented, providing for the first time a complete and accurate description of bow wave breaking at least for quasi-steady condition. After a detailed photo study of the free-surface pattern is presented, local flow measurements, including near field wave elevation, far field wave elevation and velocity measurements under the breaking waves are reported and analyzed.

The report is organized as follows: the test design is reported in chapter 2, describing the test conditions, the model geometry and the facility. Next, in chapter 3 the measurement system is reported, together with procedures and data reduction equations. Chapter 4 reports the procedures for the uncertainty analysis. Scale and Froude number effects are illustrated in chapter 5, whereas wave elevations and mean velocities measurements at Froude number 0.35 are reported and analysed in chapter 6. Complementary CFD observations are made in chapter 7 and a criterion for wave breaking detection is proposed in chapter 8. Finally, conclusions and future plans are given in chapter 9.

2. TEST DESIGN

The present experimental campaign is focused in providing detailed EFD data appropriate for physics understanding, model development and CFD validation for 3D wave breaking generated by a fast displacement ship model (surface combatant 5415).

The tests were conducted in the INSEAN basin n. 2 (fig. 1) with the 2340 INSEAN model that is 5.72 m long ($\lambda = 24.824$). Breaking wave pattern photo study for Froude number varying from $Fr = 0.28$ (design speed) and $Fr = 0.45$, including $Fr = 0.41$ (flank speed) was carried out in order to select the best Froude number for local flow measurements.

The Froude number $Fr = 0.35$ was selected in order to have a large region of wave breaking, but also a relatively steady wave pattern.

In parallel the same photo-study was conducted on the geosym 3.048 m long 5512 ($\lambda = 46.6$), at the IIHR towing tank (fig. 2) for comparison and evaluation of the scale effect, since 5512 has been used for the collection of a considerable amount of EFD data for CFD results validation, especially for unsteady flow. Full-scale photos were also used in comparison and for the evaluation of the scale effect.

Local flow measurements, including near field wave elevation, far field wave elevation and velocity measurements under the breaking waves were accomplished.

Near field wave elevation measurements were carried out from the bow to about midship using the servo-mechanic (finger) probe Kenek SH by single point measurements, which allow evaluating the mean and the rms value of the wave height.

Far field wave elevation was reconstructed by longitudinal cuts that were measured by means of an array of capacitance wire wave gauges mounted on a sliding guide as described in [1]. For these measurements, only the mean wave height was evaluated.

Three component velocity measurements were carried out by 5-hole Pitot probe in correspondence of both bow and shoulder breaking waves. The mean velocity was evaluated on four cross planes along the port side of the model.

Uncertainty assessment for wave elevation and velocity measurements were evaluated following the AIAA Standard S-071 1995.

In the following, the Cartesian frame of reference is considered fixed to the hull, with the origin at the intersection of the fore perpendicular with the undisturbed water plane. In particular, x , y and z axes are in the direction of the uniform flow, starboard side of the hull and upward, respectively. All lengths are normalized by the model length between perpendiculars $L_{PP} = 5.72$ m (INSEAN 2340 model).

2.1. Facilities

The smaller model (IIHR 5512) was tested in the IIHR towing tank (100 m long, 3.048 m wide and 3.048 m deep). The IIHR tank is equipped with an electric-motor operated drive carriage, cable driven by a 15-horsepower motor and capable of speeds of 3 m/s. Sidewall and endwall beaches enable twelve-minute intervals between carriage runs. The towing-tank water is supplied by the city of Iowa City.

The larger model (INSEAN 2340) was tested in the INSEAN basin N. 2 (220 m long, 9 m wide and 3.6 m deep). INSEAN basin N. 2 is equipped with a single drive carriage that is capable of speeds of 10 m/s. Sidewall and endwall beaches enable 20-minute intervals between carriage runs. The towing tank water is spring water.

Both the IIHR and INSEAN towing tanks use fresh water in which salinity is less than 0.5 ppt, while for the sea it is about 30 ppt. This difference mainly influences the air entrainment in the breaking waves.

All data related to the facilities and test conditions are reported in table 1.

2.2. Model Geometries

The IIHR 5512 and the INSEAN 2340 models are geosyms of the DTMB 5415 model, originally conceived as a preliminary design for a surface combatant ship. The 2340 is identical to the 5415, while 5512 is differently scaled and its length between perpendiculars is $L_{PP} = 3.048$ m. The models present a transom stern and a bulbous bow of particular shape, designed for sonar lodging. In fig. 3 the lines of the 2340 model are shown. The main geometric parameters of the two test models are given in table 2. All tests were performed in bare hull condition.

IIHR 5512 was constructed in 1996 at the DTMB model workshop from molded fiber-reinforced Plexiglas. Turbulence stimulation is at $x = 0.05$ with cylindrical studs having 3.2 mm diameter, 1.6 mm height, and 10.0 mm spacing.

INSEAN 2340 was constructed in 1998 at the INSEAN model workshop from a blank of laminated wood and a CNC machine. Turbulence stimulation is at $x = 0.05$ with cylindrical studs having 3.0 mm diameter, 3.0 mm height, and spaced 30.0 mm. The geometry offset measurement system consists of computer-aided design (CAD), hand-cut templates, level table, right angle, plumb, and rulers and feeler gauges. The data is reduced by computing crossplane and global average values for the error in the offsets for each coordinate and for S.

2.3. Conditions

Reproducing ship breaking waves in the towing tank needs accurate control over many parameters and test conditions, leading to a high repeatability of the flow. Nevertheless, the inherent disadvantage of laboratory experiments is the effect of surface tension on the breaking. Indeed, depending on the size and on the speed of the model, surface tension effects can prevent the wave to overturn and may significantly reduce the air entrainment. At all events, photographic studies were done at INSEAN and IIHR on both the 5512 and 2340 models with the aim of documenting the scale effect on the wave breaking and choosing for 2340 the best test conditions for the wave elevation and velocity measurements.

As a result of the visualizations quite steady, well-developed breaking conditions were found in the Froude number range 0.3 – 0.4. At $Fr = 0.3$ the flow

pattern was almost completely steady, but the breaking extent was not very large and its intensity was not very high. On the opposite, at $Fr = 0.41$, the wave breaking extent and intensity were respectively larger and higher, whereas the flow pattern was observed to be less steady. Eventually, Froude number 0.35 was selected for the experimental campaigns as a trade-off among the opposite needs.

During the tests, the model was held fixed, with trim and sinkage (tab. 3) set to the values previously determined in unrestrained conditions [1]. The experimental conditions correspond to Froude number $Fr = 0.35$, Weber number $We = 734$ and Reynolds number $Re = 1.5 \times 10^7$ based on free stream velocity $U_0 = 2.621$ m/s, local gravity acceleration $g = 9.8033$ m/s², water density $\rho = 998.5$ kg/m³, kinematic viscosity $\nu = 1.09 \times 10^{-6}$ m²/s, surface tension $\sigma = 0.0734$ N/m and salinity < 0.5 ppt.

3. MEASUREMENT SYSTEMS, PROCEDURES, LOCATIONS AND DRE

3.1. Photo Study

The photo study was made both at IIHR (with the 5512 model) and at INSEAN (with the 2340 model). Photos of the free surface around the bow were taken in order to observe the topology of the bow breaking wave and evaluate the scale effect on the breaking itself. The photos were made for a wide range of Froude numbers, but here only those taken at moderate and high Froude numbers are shown, for which the wave breaking is clearly observable for both model scales ($Fr = 0.28, 0.3, 0.325, 0.35, 0.375, 0.41$ and 0.45). For $Fr = 0.28$ and $Fr = 0.35$, photos of the full scale (DDG 51) are also shown for comparison.

3.2. Wave Elevations

The wave height was measured by a servo-mechanic probe (Kenek SH), mounted on a system of guides fixed to the carriage. The wave field was obtained by point wise measurements from the bow down to about midship.

In order to get wave elevation measurements as close as possible to the hull, some part of the port side of the model was cut off as shown in fig. 4.

The carriage acceleration was lowered as much as possible in order to reduce the wave fluctuations due to the transient wave components. Time history and running mean and rms value for a measuring point inside the breaking region ($x = 0.15$, $y = -0.09$) are shown in figure 5. Both mean and rms converged to an asymptotic value

quite rapidly. This allowed setting the acquisition time interval to $t_a^{NF} = 2.2 \text{ s}$ with a sampling rate $f_s^{NF} = 1000 \text{ Hz}$. The Near Field free surface measurements were carried out at the vertices of a regular grid with spacing $\Delta x^{NF} = 4 \text{ cm} \cong 0.007 L_{PP}$, $\Delta y^{NF} = 2 \text{ cm} \cong 0.0035 L_{PP}$. The longitudinal displacements (4 cm) were set by hand, while the transverse ones (2 cm) were automatically actuated by a transverse guide equipped with a step motor controlled by software made at INSEAN. The used step-motor has a resolution of 200 steps per revolution and the maneuvering screw of the guide has a pitch of 10 mm. Thus, the accuracy of the transverse displacements is 0.05 mm.

To complete the wave pattern, a Far Field region was investigated by capacitance wires, although in this part of the wave pattern the rms value of the wave elevation was not measured. The distance between the longitudinal cuts was $\Delta y^{FF} = 0.0017 L_{PP}$, while the x-step derived by the sample rate ($f_s^{FF} = 300 \text{ Hz}$) and the carriage velocity ($U_0 = 2.621 \text{ m/s}$), being $\Delta x^{FF} = U_0 / f_s^{FF} \cong 0.0015 L_{PP}$. In figure 6, the measured area by finger probe is shown together with the area investigated by means of capacitance wires.

3.3. Mean Velocities

Velocity field was measured on the port side, at the x-stations located 0.15, 0.2, 0.4 and 0.5 L_{PP} downstream the fore perpendicular. A 5-hole Pitot wake probe was used being less intrusive than the boundary layer probe used for the flow map at $Fr = 0.28$ [3]. Classical Pitot tube was used to measure the static pressure in the undisturbed flow region, far enough from the model. Five differential pressure transducers (Valydine DP15) were connected to the five Pitot holes and to the static pressure hole of the Pitot tube.

The acquisition system runs automatically, guided by the same software used for the Near Field wave measurements. In this case, two orthogonal guides, actuated by two step-motors, drove the Pitot to the measuring point, starting from a reference position. The two step-motors have a resolution of 200 steps per revolution and the maneuvering screw has a pitch of 10 mm, so that the spatial resolution of the device is 0.05 mm in vertical and transverse direction.

Before starting the acquisition and during the acquisition itself the carriage speed signal was checked by the software. When the signal was within a pre-defined range (± 2.5 cm/s), the acquisition started. At the end of the acquisition, the system moved the Pitot probe to the next measuring point.

A regular grid with square cells, whose side dimensions were $\Delta x_g^V = \Delta z_g^V = 0.0025 L_{pp}$, was drawn just below the free surface. The adopted sampling rate was $f_s^V = 100$ Hz and the acquisition time interval was set to $t_a^V = 4 \sim 6$ s, depending on the distance from the free surface, in accordance with a previous analysis performed to determine the time needed to have a steady average (Fig. 7). Three-velocity components and pressure coefficient, at each point, were calculated through the calibration maps, with real time preview.

In the following, the velocity components are indicated as u (axial), v (transverse) and w (vertical), respectively. They are normalized by the nominal velocity (carriage velocity) $U_0 = 2.621$ m/s. In figure 8.a the measuring grid used for the mid-ship section $x = 0.5$ is represented together with the corresponding transverse wave cut and the hull boundary. In figure 8.b only the properly acquired points are shown.

As previously mentioned, the velocity field was measured on four cross-sections just downstream the bow wave front ($x = 0.15$ and $x = 0.2$) and around mid-ship ($x = 0.4$ and $x = 0.5$). The analyzed sections were chosen in order to investigate the flow produced by both the bow and shoulder wave breaking. The $x = 0.15$ and $x = 0.2$ sections were chosen in order to investigate the flow produced by the bow breaking wave. The $x = 0.4$ section is the only one in which both the resulting flow from the bow breaking wave and the shoulder breaking wave are included. The mid-ship section $x = 0.5$ was selected to examine the flow in correspondence of the shoulder breaking wave.

The position of the investigated cross sections with respect to the wave field is summarized in fig. 9.

3.4. Data Reduction Equations

Wave elevation h was measured with a servo-based measurement systems and PC data acquisition. The DRE is

$$h = \frac{K_K(e - e_0)}{L_{PP}}, \quad (1)$$

where e is the voltage output acquired by the PC and K_K is the calibration coefficient. e_0 is the voltage output related to the undisturbed free surface; it is acquired before every carriage run.

The measurement system consisted of a Kenek SH servo- mechanic probe, signal conditioner, 2D traversing system, 12-bit AD card and carriage PC. The servo probe, signal conditioner, and carriage PC AD card were statically calibrated on the traverse system to determine the voltage-wave elevation relationship.

Velocity fields data (u , v , w , C_p ; $x = 0.15$, $x = 0.2$, $x = 0.4$, $x = 0.5$) were measured by 5-hole Pitot probe/differential pressure transducer based measurement system and PC data acquisition. The DREs are

$$u(x, y, z) = (VX \cos \alpha_p \cos \phi_p + VY \sin \phi_p + VZ \sin \alpha_p \cos \phi_p) / U_c \quad (2)$$

$$v(x, y, z) = (-VX \cos \alpha_p \sin \phi_p + VY \cos \phi_p - VZ \sin \alpha_p \sin \phi_p) / U_c \quad (3)$$

$$w(x, y, z) = (VZ \cos \alpha_p - VX \sin \alpha_p) / U_c \quad (4)$$

$$C_p(x, y, z) = \frac{2(p - p_o)}{\rho U_c^2} = \frac{2H'_c - \rho P V'^2}{\rho U_c^2} \quad (5)$$

where,

$$VX = V' \cos \phi \cos \alpha \quad (6)$$

$$VY = V' \sin \phi \quad (7)$$

$$VZ = V' \cos \phi \sin \alpha \quad (8)$$

$$V' = \sqrt{\frac{2M'}{\rho M}} \quad (9)$$

$$M' = 4H'_c - H'_t - H'_b - H'_p - H'_s \quad (10)$$

$$K' = \frac{H'_t - H'_b}{(4H'_c - H'_t - H'_b - H'_p - H'_s)} \quad (11)$$

$$L' = \frac{H'_s - H'_p}{(4H'_c - H'_t - H'_b - H'_p - H'_s)} \quad (12)$$

(α_p, ϕ_p) are the 5-hole Pitot probe preset pitch and yaw angles, respectively, (α, ϕ) are the measured pitch and yaw angles of the velocity vector in 5-hole Pitot

probe coordinates, respectively, and H'_j , ($j = c, t, b, p, s$) are the measured pressures for the center, top, bottom, port, and starboard holes, respectively. The side holes of the static Pitot probe measured the reference pressure (p_0).

The primed variables designate the local measured values and coefficients computed using local measured values, whereas, unprimed variables (K, L, M, P) designate variables from a wind tunnel calibration of the 5-hole Pitot probe [1]. (α, ϕ) are obtained from (K', L') and their corresponding 5-hole Pitot probe calibration coefficients (K, L). (α, ϕ) are then used to obtain (M, P) from their corresponding 5-hole Pitot probe calibration coefficients.

4. UNCERTAINTY ASSESSMENT

Uncertainty assessment of the results was carried out following the AIAA Standards S-071-1995 [4] for both wave elevation and velocity.

The bias limit was evaluated by taking into account the more important sources of error. The precision limit was evaluated by 10 repeated tests for both wave elevation and velocity measurements.

4.1. Wave Elevations

Wave elevation was measured in the near field using a Kenek SH servo-mechanic probe, which DRE is

$$h = \frac{K_K(e - e_0)}{L_{pp}} \quad (1)$$

The bias limit was evaluated based on the propagation of the elemental biases into the wave elevation bias, while the precision limit was evaluated on 10 repeated tests directly on the wave elevation data.

The wave elevation depends on a series of variables including the measuring point and the carriage velocity U_0 :

$$h = f(K_K, e, e_0, L_{pp}, x, y, U_0) \quad (13)$$

The sensitivity coefficients are:

$$\theta_{K_K} = \frac{\partial h}{\partial K_K} = \frac{e - e_0}{L_{pp}} \quad (14)$$

$$\theta_e = \frac{\partial h}{\partial e} = \frac{K_K}{L_{pp}} \quad (15)$$

$$\theta_{e_0} = \frac{\partial h}{\partial e_0} = -\frac{K_K}{L_{pp}} \quad (16)$$

$$\theta_{L_{pp}} = \frac{\partial h}{\partial L_{pp}} = -\frac{1}{L_{pp}} \cdot h = -\frac{K_K(e - e_0)}{L_{pp}^2} \quad (17)$$

The sensitivity coefficients related to the measuring point coordinates are obtained deriving the acquired data using finite differences;

$$\theta_x = \frac{\partial h}{\partial x} \quad (18)$$

$$\theta_y = \frac{\partial h}{\partial y} \quad (19)$$

The last term,

$$\theta_{U_0} = \frac{\partial h}{\partial U_0} \quad (20)$$

should be determined by performing the test at different velocities for the measured field. Nonetheless being the velocity bias very small ($\cong 3$ mm/s [5]), this term was neglected in the estimation of the bias limit. The precision limit was determined directly on h.

4.1.1 Bias Limit The bias on e and e_0 was obtained by the ratio between the voltage range of the acquisition board (± 10 V) and its resolution (2^{12}). This value was normalized with the used range by the sensor that was $\Delta e = \pm 3$ V. Being this bias present both on e and on e_0 , the total bias due to the A/D conversion is obtained by:

$$B_{A/D} = \sqrt{2} B_e \quad (21)$$

The bias on KK is given by the manufacturer of the sensor as 0.2% and it was checked before and after the tests (B_K in tab. 4).

The bias on the model length is $B_{LPP} = 1$ mm [1] and it was considered negligible with respect to the other elemental biases.

The biases on x and y, which individuate the measuring point, were determined considering the sequence of the needed measurements in order to set the position of the sensor in the model reference frame ($B_x = 0.707$ mm, $B_y = 0.866$ mm).

The evaluation of the sensor position with respect to the model, involves many difficult measurements, including the use of tools such as squares and plumb line. For this reason, we decided to dismount the model and the sensor every time we performed a carriage run for the precision limit evaluation. In this way, the errors on the measuring point were transformed in random-type errors and they were automatically included in the h precision limit.

4.1.2 Precision Limit The precision limit was determined in three different points located in the non-breaking, close to the breaking and breaking region respectively. The locations of the three points are reported in table 4 together with the values of the considered biases $B_{A/D}$ and B_{KK} , the precision limits and the total uncertainties for the mean and for the rms value of the wave elevation.

4.2. Mean Velocities

The bias limit on the velocity was determined following the procedure elaborated in [1]. Elemental errors associated to the 5 pressure values given by the Pitot, the Pitot position with respect to the model, the preset angles, the flow angles, the carriage velocity, P and M coefficients [1] and velocity gradient [3] were considered to estimate the bias limit. Its value is comparable with the ones obtained in a previous study on the boundary layer flow of the same model at $Fr = 0.28$ [1]. The precision limit was determined directly on the three velocity components for a measuring point at section $x = 0.20$, just under the breaking ($y = -0.1015$, $z = -0.005$). The precision values are also comparable with the ones of the $Fr = 0.28$ boundary layer data. Here the percentage values are lower just because of the larger range of variation of the transverse and vertical velocity components.

Bias limit, precision limit and total uncertainty for the point located at $x = 0.20$, $y = -0.1015$, $z = -0.005$, are given in table 5.

5. FROUDE NUMBER AND SCALE EFFECTS

For the purposes of this paper, the photo study of the wave breaking generated by the two scaled models and performed at moderate and high Froude numbers ($Fr = 0.28, 0.3, 0.325, 0.35, 0.375, 0.41$ and 0.45) using same perspective views was compared with full scale pictures at $Fr = 0.28$ and $Fr = 0.35$. Throughout the series of

pictures the influence of the physical quantities and the main nondimensional parameters on the wave breaking are studied.

The lowest analyzed speed is $Fr = 0.28$. 5512 (figs. 10.a, 10.b) shows small regions of bow wave curling and spilling-type breaking with capillary waves along toe and shoulder wave with roughened crest region with capillary waves hinting at spilling-type breaking wave. Model 2340 (figs. 10.c, 10.d) shows more curling and developed spilling-type bow wave breaking. The role of the surface tension is shown by the enlarged view in fig. 10.e. Moving downstream with the flow, the breaking grows in amplitude and ripples become visible just upstream the wave “toe” [2]. The shoulder wave breaking (not visible in fig. 10.c and 10.d) resembles a 2D spilling wave breaking as per model 5512 but with higher intensity.

For $Fr = 0.28$, photos of the full scale are shown for comparison. Figure 10.g shows that differently from both models, the real ship bow wave is a spilling type breaking with generation of spray, splash and droplets, which lead to a significant production of white water. The shoulder wave is also a spilling breaker type with generation of whitewater along crest.

For $Fr = 0.3$ and $Fr = 0.325$, both 5512 and 2340 results are similar to those of $Fr = 0.28$ but with increased regions and curling of bow wave close to hull especially for 2340 and two small scar lines along back of bow wave for 2340.

In particular, at $Fr = 0.3$, model 5512 shows (fig. 11.b) a slightly intense bow wave breaking, still affected by the action of the surface tension. The shoulder wave breaking (fig. 11.a, 11.b) is quite similar to the one observed at $Fr = 0.28$, with the crest swept back more than in the previous case. Small scars begin to form just behind the bow breaking (fig. 11.a). Model 2340 shows a more intense bow wave breaking with respect to $Fr = 0.28$ and streamlined scars begin to appear on the free surface (fig. 11.c). These will become more visible at higher Froude numbers.

At $Fr = 0.325$ (fig. 12) the breaking scenario is quite similar to the one observed at $Fr = 0.3$ for both models, although a number of details begin now to emerge. By comparing fig. 11.a and 12.a, it can be seen that the bow breaking is now more intense and the wake left behind by the breaker extends further normally to the wave front, i.e. toward the hull for the 5512. Likewise, in fig 12.a, small scale surface disturbances left by the breaking appear on the left of the bow wave, covering a wider area behind the breaking front. For the 2340, scars are also more pronounced although they disappear rapidly downstream (fig. 12.c).

At $Fr = 0.35$ (fig. 13) more details are clearly identifiable and the whole picture is compared to full scale visualization. Model 5512 exhibits (fig. 13.b) a bow breaking wave. Moving along the crest of the bow wave, the wave front begins to rise at the extreme bow and a bulge grows onto the top of the bow wave. The air entrainment is strongly limited by the action of the surface tension.

Figures 13.c and 13.d show the downstream and upstream perspective of the bow breaking wave for the 2340 model. 2340 shows large regions of bow wave almost steady plunging breaking close to hull and spilling breaking further from hull. Also visible are two large scars downstream of the bow wave and a large region shoulder wave spilling breaker. Full scale shows spilling breaking bow wave with white water along crest and back merging with shoulder wave both with splash, initially plunging and then becoming spilling. Fig. 14.a shows the rise of the free surface at the extreme bow and overturn of the wave crest. Fig. 14.b shows scars on back of breaking bow wave. These scars extend downstream to about midship (figs. 14.c and 14.d). The shoulder wave exhibits a low energetic content developing a “2D spilling”-like wave breaking as shown in figure 14.d. The wave breaking scenario observed for the 2340 qualitatively resembles the full scale scenario except for the amount of generated white water (figs. 13.e and 13.f).

For $Fr = 0.375$, 0.41 and 0.45 , both 5512 and 2340 photos show similar incremental trends as per $Fr=0.35$, including large effects unsteady flow (e.g. ejections, etc.).

At $Fr = 0.375$ the 5512 shows (fig. 15.a and 15.b) a quite developed spilling bow breaker. The shoulder wave is merging with the hull. The near field generated by the 2340 is quite similar to the previous case ($Fr = 0.35$), except for the presence of stronger water ejections.

At $Fr = 0.41$ (fig. 16) the bow wave breaking of the 5512 appears in form of plunging breaker. Air entrainment is considerably increased in this case, but looking to the starboard side, differences between 15.a and 15.c show that the role of the surface tension for the smaller model is still relevant. For the 2340, overturns are quite evident and the plunging nature of the breaker is clearly visible in figure 16.c.

At $Fr = 0.45$ (fig. 17) the bow wave breaking of the 5512 is characterized by the presence of both plunging-type breaker (upstream) and spilling-type breaker (downstream) as shown in figure 17.b. The bow wave breaking of the 2340 is entirely

plunging-type and generates a system of streamlined rolls that evolve along the hull (Fig. 17.c).

As a summary of the photo study we can state that scale effects in wave breaking are significant when comparing 5512 scenario vs. 2340, with increasing differences for increasing Fr. Scale effects are still observable for 2340 vs. full scale although some particular features of the full scale flow are reproduced by the 2340 model wave breaking. $Fr = 0.35$ is the first speed with a quite steady, well developed breaking with a sufficiently high energetic content. For Froude numbers higher than $Fr = 0.375$ unsteadiness appears and the bow breaking wave generates strong water ejections that made the measurements troublesome. Consequently, $Fr = 0.35$ was finally selected for the near wave field and the velocity measurements for the 2340 model.

5.1. Surface Tension and Viscous Effects

In the following, based on the photo study and literature results about waves and wave breaking, the physical quantities that influence the wave breaking development in model scaled experiments are analyzed.

As known from literature, small scale wave breaking is strongly influenced by surface tension [2,16]. Furthermore, the wave breaking is intimately connected with turbulence generation that is a viscous phenomenon. Hence, the parameters to be considered other than Froude number (Fr), are at least, Weber number (We) and Reynolds number (Re), whose definitions are:

$$Fr = \frac{U}{\sqrt{gL}} \quad (22);$$

$$We = U \sqrt{\frac{\rho L}{\sigma}} \quad (23);$$

$$Re = \frac{UL}{\nu} \quad (24).$$

being U and L the model speed and length, g the gravity acceleration, ρ and ν the fluid density and kinematic viscosity and σ the water-air interface surface tension. In table 6 the Froude, Weber and Reynolds numbers for 5512, 2340 and full scale are given for all the analyzed conditions, while the corresponding physical quantities are listed in table 7.

In order to satisfy the Froude similarity, the scaled model experiments are performed at a lower velocity with respect to the full scale and this automatically implies the violation of the Weber and Reynolds similarity. It is then fundamental to assess experimental conditions in which surface tension and viscous effects do not change too much the wave breaking characteristics at model scale, with respect to the applications (full scale). To this aim, important indications may be gathered from the photo study described before.

Because the surface tension term depend on the magnitude of the radius of curvature of the free surface, the role played by surface tension may be quite different for breaking and non breaking (regular) waves, and in the latter case it is also of relevance the wavelength. In a previous work [17], Stern et al. focused on comparing resistance, sinkage and trim, and wave pattern measurements on the same model geometry (the DTMB 5415) between three institutes (two of the institutes used 5.72 m models whereas the third used a smaller 3.048 m model). Scale effects for the smaller model were only evident for resistance and trim tests for $Fr > 0.26$ and $Fr > 0.33$, respectively, while in the low Froude number range, corresponding to a non-breaking wave pattern, scale effects were found to be almost negligible. In the present campaign, the photo study revealed that the smaller scale experiment does not generate a developed breaking for Froude number lower than $Fr = 0.41$ ($We = 456$, see table 6), while the larger scale experiment exhibits a well developed breaking starting from $Fr = 0.3$ ($We = 627$).

A further analysis has been carried out the considering the wavelengths of the diverging wave systems as reference lengths in the Weber number (We_λ). The values of these wavelengths are reported in table 8 together with the corresponding Weber numbers (We_λ)¹. As observed in the photo study, for the smaller model (5512), the surface tension is less dominant in the wave breaking for $Fr > 0.41$, while for the larger one (2340), its effect is present up to $Fr = 0.3$. It is noticeable that the limiting condition corresponds for both cases to wavelengths of the diverging waves of 41 cm and velocity of 2.24 m/s. The related Weber number We_λ is in both cases $We_\lambda = 168$.

It is interesting to notice that, although the minimum wavelength needed in order to have pure gravity waves is about 1 m [16], is commonly accepted that for

¹ In table 8 the λ^{DW} value of the 2340 model at $Fr = 0.35$ is obtained from the experimental data, and serves as a base for calculating all the other values for different Froude numbers and model lengths.

wavelength larger than 40 cm the effect of the surface tension can be neglected², in agreement with present findings.

Furthermore, the influence of the viscosity should be considered.

The Reynolds number for the full scale is about two orders of magnitude larger than the model Reynolds number. Furthermore, being the first stage of the breaking generated at the bow, a local Reynolds number (e.g. based on the axial abscissa x) has to be considered in order to relate the wave breaking with viscous phenomena, with particular attention to the laminar/turbulent transition. Considering the critical Reynolds number for the flat plate ($Re_c \cong 3.5 \times 10^5$), the smaller model flow undergoes the laminar/turbulent transition at about $x = 0.05$ at the maximum speed ($Fr = 0.45$) and $x = 0.08$ at $Fr = 0.28$, whereas the flow around the larger model undergoes the turbulent transition at $x = 0.02$ at $Fr = 0.45$ and $x = 0.03$ at $Fr = 0.28$. The full scale flow is turbulent for $x > 0.005$.

On the other hand, it has to be noticed both models are provided by turbulence stimulators placed at $x = 0.05$.

Nonetheless, figures 10.a and 10.b show that wave breaking at $Fr = 0.28$ for the 5512 starts to develop downstream with respect to the 2340 and this could be related to the low Re nature of the flow around the 5512 upstream $x = 0.08$.

Furthermore, figures 10-17 show that the bow wave breaking of the 2340 generates free surface turbulence for all the analyzed cases, while 5512 generates free surface turbulent flow only for $Fr \geq 0.41$. Moreover, the scars generated by 2340 at $Fr = 0.35$ are clearly turbulent (fig. 14), whereas the scars generated by 5512 appear to be laminar (figs. 11.a - 17.a).

A better indication on the importance of the viscous dissipation in the wave breaking development should be given by the (local) turbulent Reynolds number, based on the intensity of the velocity fluctuations and Taylor micro-scale [8]. However, the estimate of this parameter requires the use of a different system for the velocity measurement, as PIV, LDV or hot-film anemometer and it cannot be obtained with present data.

² Experimental results obtained by Duncan for 2D waves produced by a submerged hydrofoil gave a wavelength of about 41 cm [7] and have been often taken as a reference benchmark in the development and validation of numerical codes not taking into account surface tension forces.

Another aspect that should be analyzed is the difference in salinity between the seawater and the water used for the experiments. In fact, salinity changes the density and consequently Reynolds and Weber number, although, differences caused by density changes in the value of these two parameters are very small. In addition, the surface tension increases with salinity, although the role of the surface tension in the full scale breaking can be neglected, due to the large value of the waves curvature radius.

The more important effect of salinity relates with air entrainment and production of white water. In fact, the percentage of the dissolved gases decreases when salinity increases [13], so that bubble generation and air entrainment could be rather different in the laboratory wave breaking with respect to seawater wave breaking.

Nevertheless, the influence of the salinity on free surface topology and flow evolution can be considered a minor source of discrepancies between the model and the full scale breaking with respect to scale effects [18].

6. FROUDE NUMBER 0.35 WAVE ELEVATIONS AND MEAN VELOCITIES

On the basis of the previous considerations the 2340 model was selected for the wave breaking analysis focusing the measurements on the flow field at $Fr = 0.35$.

The reconstruction of the wave elevation field was done in terms of the mean value (near and far fields) and rms value (near field), whose patterns are shown in figures 18.a and 18.b. In figure 18.a, capacitance wires data are shown together with the finger probe data for the mean wave elevation. The highest value of the wave elevation in the measured field is $h_{\max} = 1.80 \cdot 10^{-2} L_{PP}$ (= 103.0 mm) and the minimum is $h_{\min} = -1.06 \cdot 10^{-2} L_{PP}$ (= 60.6 mm). The bow wave breaking is quite strong as indicated by the maximum of the rms value of the wave fluctuations that is about 1/10 of the maximum wave height $h_{rms}^{(\max)} = 1.97 \cdot 10^{-3} L_{PP}$ (= 11.3 mm). The shoulder wave breaking (spilling-type) is gentler than the bow wave breaking, as underlined by the contours of the rms values of the wave fluctuation (fig.19.b).

The analysis of the mean wave field reveals some peculiar features of the breaking. The bow wave (figs. 19.a and 20.a) displays a quite bumpy shape. The wave front breaks into three regions separated by two scars, as observed in the photo study

(figs. 13 and 14). These scars are characterized by sudden changes in the mean wave height. The first one (scar 2), closer to the hull, is more visible whereas the second (scar 1), further from the hull, appears weaker as shown in Fig. 14b and beyond which there is a region characterized by high free surface turbulence. Their location is indicated in figures 19.a and 19.b and figures 20.a and 20.b, where the mean value and the rms value of the wave height are shown together with the transverse wave cuts used for the wave pattern reconstruction. The two scars are both characterized by relatively high values of the wave fluctuations as shown in figure 20.b, where the rms value of the wave elevation is shown.

Figures 21 and 22 show the velocity measurements under the bow wave in terms of axial velocity contours and cross flow vectors (figs 21.a and 22.a) and axial vorticity contours (21.b and 22.b).

Figures 21.a and 21.b relate to cross section $x = 0.15$. Axial velocity defect under the bow wave crest is noticed in correspondence of high cross flow (fig. 21.a). Clockwise (negative) vorticity is present under the breaking bow wave. A small region of positive (counterclockwise) vorticity is also shown nearby the scar 1 (fig. 21.b). Unfortunately, due to the dimension of the 5-hole Pitot head and the unsteadiness of the free surface, it was not possible to reach the free surface in order to complete the velocity field, and part of the vorticity dynamics is missing in the present analysis.

Figures 22.a and 22.b relate to cross section $x = 0.20$. As for section $x = 0.15$, the flow at section $x = 0.20$ exhibits an axial velocity defect under the bow wave crest in correspondence of high cross flow (fig. 22.a). The vorticity pattern is also very similar to $x = 0.15$, although positive vorticity is observed here, under the clockwise (negative) vortex (fig. 22.b). As for section $x = 0.15$, the measurements could not reach the free surface and not all the vorticity is highlighted by present data. It is reasonable to presume that positive vorticity has to be present close to the negative vorticity region. To answer this question CFD results obtained by RANS code will be used to complete the EFD data.

The dynamics of the shoulder wave breaking appears to be completely different from the bow wave breaking. In particular, as shown by the picture in figure 14.d, the shoulder wave breaking is spilling-type and the contours of the rms value of the wave elevation in fig. 19.b show that in the near field the wave front develops along a straight line inclined of about 19° with respect to the x-axis.

Figures 23.a and 23.b relate to cross section $x = 0.40$. Figure 23.a shows the cross flow vectors and axial velocity contours under the shoulder wave crest, the bow wave trough and part of the velocity field related to the bow wave crest ($y \lesssim 0.16$).

As for the bow wave crest, the axial velocity under the shoulder wave has a local minimum, whereas, moving outboard, the axial velocity exhibits a local maximum, in correspondence of the bow wave trough. The flow under the bow wave crest ($y \lesssim 0.16$) is still characterized by low axial velocity, as for the upstream sections $x = 0.15$ and $x = 0.2$.

Figure 23.b shows the axial vorticity patterns. Two clearly defined regions of negative vorticity are visible under the shoulder wave crest ($y = 0.085, z \approx 0.01$) and ($y = 0.11, z \approx 0.01$), while closer to the free surface a thin region of positive vorticity is noticed ($y = 0.09, z \approx 0.008$). Moving outboard, very close the free surface, a thin strip of negative vorticity is shown, which ends nearby the bow wave crest, where a region of positive vorticity is observed ($y = 0.195, z \approx 0.005$).

Figures 24.a and 24.b show the flow pattern at $x = 0.5$. As for section $x = 0.4$ the axial velocity under the shoulder wave crest has a local minimum with high cross flow close to the breaker. The flow under the bow wave trough shows a maximum of the axial velocity (fig. 24.a).

The axial vorticity pattern shows two negative vortices located at ($y = 0.085, z \approx 0.01$) and ($y = 0.11, z \approx 0.01$) as for section $x = 0.4$, whereas the positive vorticity is visible at ($y = 0.12, z \approx 0.06$). It has to be mentioned that, although the closest vectors to free surface were not used for the vorticity calculations, it is presumed that the vorticity very close to the free surface could be affected by higher uncertainty than in the rest of the measured field and some boundary effects could compromise the results on the points close to the free surface.

The shoulder wave flow exhibits some similarities with a 2D spilling breaker, although a fundamental difference occurs in the 3D scenario. In a 2D breaking, the flow direction is normal to the wave front (aligned with the wave vector), whereas in the present case the flow direction and the wave front form an angle of about 19° , being the flow almost aligned with the x-axis. This difference likely does not affect the mechanism responsible for the vorticity production at the toe of the wave breaking, but it plays a fundamental role in the vorticity convection and evolution. Indeed, in a 2D breaker the vorticity produced at the toe can only be convected downstream, normally to the wave front generating a 2D shear layer. On the opposite, in the 3D case the

gradient of the velocity along the wave front can stretch the eddy generated at the breaking. This mechanism can affect the vorticity intensity and consequently the breaker intensity, whereas the propagation of the vorticity normal to the wave front is very slow.

7. COMPLEMENTARY CFD OBSERVATIONS.

Concurrently to the described experimental campaign, a CFD simulation of the same flow was carried out at IIHR using CFDSHIP IOWA RANS code, which is described in details in [19].

Here, CFD data will be used to fill the EFD data in order to better understand the flow under the bow and shoulder wave breaking, prior verification of the agreement of the CFD results with EFD data in the measured regions. In fact, as previously mentioned, it was not possible to measure very close to the free surface, due to the free surface unsteadiness and dimensions of the Pitot head.

7.1. Free-Surface Wave Field and Flow.

A comparison of wave elevation contours with measurements at $Fr = 0.35$ is provided in Figure 25, where the CFD prediction is able to capture the height of the overturning bow and shoulder waves. The main differences are that the bow wave height of the CFD prediction is underpredicted (i.e., the breaking is not as strong as in the data) and the wavelength is shorter in comparison with the data. Figure 26 provides a comparison of a photograph of the bow wave around the ship model and free-surface perturbation streamlines from the CFD prediction (i.e., streamlines in an earth-fixed coordinate system where the forward speed of the ship is subtracted from the axial velocity). As indicated in the photograph, two “scars” on the free surface interface can be observed (i.e., small-scale depressions in the free surface, which originate downstream of the breaking bow wave and are aligned with the axial direction). The location of the scars correlates with the location of the converging and diverging perturbation streamline pattern in the CFD simulation. Figure 27 shows that the effect of the trough in between the bow and shoulder waves ($0.2 < x < 0.5$) is to generate a favorable pressure gradient normal to the trough line, which accelerates the axial flow and turns the flow towards the hull giving the observed streamline pattern (i.e., axial velocity greater than the free stream value and negative transverse velocity). It is this

sharp transition region, between the outward flow caused by the forebody and the inward accelerating flow at the trough, which generates the diverging free surface streamlines denoted as scar 1 in Figure 26. Downstream of the trough line, the flow experiences an adverse pressure gradient and decelerates, eventually reversing sign as seen at the shoulder wave in Figure 27 (i.e., the axial and transverse perturbation velocity become negative and positive, respectively). The reversal of the perturbation flow in between the trough and the shoulder wave results in a set of converging free surface streamlines (denoted as scar 2 in Figure 26).

Although there is a correlation between the experimentally observed scars and the perturbation streamlines, small scale depressions in the free-surface elevation are not observed in the CFD simulations. Two possible explanations are that (i) the CFD grid is very coarse in comparison to the scale of the scars and/or (ii) there is no surface tension in the CFD calculations so we do not resolve the capillary waves on the free surface.

As a matter of fact, even in the EFD wave elevation data, which measurement grid is finer than the CFD grid, scars are not easy to recognize, especially downstream the bow wave crest ($x > 0.2$). Additional research is required to determine the mechanism for the generation of the scars. Future measurements and simulations may be able to resolve the scars if the measurement and computational grids are extremely fine.

7.2. Boundary Layer and Free-Surface Vortices.

Here, the CFD results are shown in terms of axial velocity and vorticity contours at the four experimentally investigated cross sections $x = 0.15$, $x = 0.20$, $x = 0.40$ and $x = 0.50$. The used code is able to accurately predict the “wake” of the low speed fluid at the free surface downstream of the overturning bow wave ($x = 0.15$ and $x = 0.20$). Also, the acceleration of the axial velocity by the trough in between the bow and shoulder wave is correctly predicted at $x = 0.40$ and $x = 0.50$. Comparisons of the axial vorticity shows good agreement with experimental measurements with respect to the magnitude, location, and content of the free surface vortices (Figs 28 a-d and 29 a-d), giving also much more information on the flow very close to the free surface.

Based on their good agreement with the EFD data, the CFD results can be used to fill-in the sparse experimental dataset in order to understand the effects of the overturning bow wave on the downstream flow.

To this purpose, free surface elevation and axial vorticity contours are shown in figure 30 from CFD, where five free surface vortices are identified and labeled as V1÷V5. The location of the vortex cores was found by tracing the center of closed contours of axial vorticity from $0.1 < x < 0.6$.

Form the whole field picture emerges that V1 and V4 are associated with the overturning bow wave, while V2, V3, and V5 are associated with the shoulder wave.

It is clear that measurements are able only to highlight clearly V1 and V2, while only traces of V4 and V5 can be recognized on figures 29 (a, b, c) and figures 29 (c, d) respectively.

Present work represents a good example of synergy between EFD and CFD. In fact, we used EFD in order to validate CFD and successively CFD results in order to fill-in the sparse experimental dataset, giving a complete picture of the analyzed flow.

8. A 3D BREAKING DETECTION CRITERION.

As observed in the photo study (fig. 14 d) and then measured (fig. 19.b), the shoulder wave breaking closely resemble a 2D spilling breaking. As known by literature (Duncan, [7]), the inception of 2D spilling breaking can be predicted based on the ratio between wave amplitude and wavelength ($2a/\lambda \cong 0.1$) of a regular wave train. This criterion can be also expressed based on the related local steepness $\theta = 17.1^\circ \pm 1.2^\circ$ [7].

This second form of the 2D criterion can be in principle extended to complex 3D wave fields as the one examined in the present study.

Here, the wave steepness was determined by derivative of the mean wave elevation normal to the wave front and it is shown in figure 25 (top). In the figure only the 0° and 17° contours are shown, in order to localize better the breaking regions predicted by the criterion. In the bottom plot of fig. 25, the rms value of the wave elevation is represented in order to highlight the breaking region.

The comparison of the two plots in figure 25 shows that the $\theta = 17^\circ$ criterion seems to predict correctly the inception of the breaking, suggesting the usefulness of

the extension of the “local form” of the 2D criterion to 3D wave fields, at least for spilling breakers.

9. Conclusions and Future Work

This report represents an advanced example of how complementary EFD and CFD can provide a powerful and advanced tool in analyzing complex industrial flows by completing and validating each other.

The results of an experimental campaign performed in collaboration at INSEAN, using INSEAN model 2340A (exact geosym of the DTMB 5415) and at IIHR, using DTMB model 5512 (3.038 m, 1/46.6 scale geosym of 5415) are reported. The project was aimed at measuring 3D wave breaking generated by a fast displacement surface combatant. The purpose was to provide detailed EFD data for appropriate physics understanding as well as model development and CFD validation.

A careful photo study proved to be of great help in fixing the test conditions ($Fr = 0.35$) and in putting in evidence some peculiar features of the free-surface flow, namely “scars”. Mean and rms values for the near field wave elevations were measured, whereas the far field was reconstructed with mean values only. Velocity measurements under the bow and shoulder waves were conducted in four transversal sections and the axial vorticity contours were also reconstructed, highlighting vortex structures near the free-surface (WB vortices).

CFD simulations were used to complete the experimental data, allowing to give a complete picture of the flow field under bow and shoulder waves and to identify free-surface scars through the use of free-surface streamlines.

Present experimental data are among the most accurate and detailed measurements of this type of flow and the authors believe that they will be of relevance in CFD benchmarking. The analysis carried out demonstrated the richness of the flow field under breaking waves. Current developments and future work include more detailed computations in the free surface breaking region, making use of level set approaches (to deal with large deformation and breaking of the free surface) and chimera or overlapping grids for fine grid resolution.

From the experimental standpoint, the role of scale effects and surface tension still need to be investigated beyond the present point. To this aim F. Pistani dedicated his Ph.D. thesis [21] to measuring the flow field about a very large model of the 5415.

The scale adopted ($\lambda=14.32$, for a model length of $L_{pp}=9.916$ m) is sufficiently large for the model divergent wave system to be negligibly affected by the surface tension forces. At the moment the thesis is almost completed and the authors of the present report believe that these data will represent a useful integration of the data reported here and will help in further understanding ship breaking wave flows.

REFERENCES

1. OLIVIERI, A., PISTANI, F., AVANZINI, G., STERN, F. AND PENNA, R. 2001; Towing Tank Experiments of Resistance, Sinkage and Trim, Boundary Layer, Wake and Free Surface Flow around a naval combatant INSEAN 2340 Model. IIHR Report No. 421.
2. LONGUET-HIGGINS, M.S., 1996; Progress towards understanding how waves break. 21st Symposium on Naval Hydrodynamics, Trondheim, Norway.
3. OLIVIERI, A., PISTANI, F., AND PENNA, R. 2003; Experimental investigation of the flow around a fast displacement ship hull model. *J. Ship. Res.*, 47, 3 pp.247-261.
4. COLEMAN, H.W., STEELE, W.G., 1995; Engineering Application of Experimental Uncertainty Analysis. *AIAA Journal*, **33**, 10, 1888-1895.
5. AVANZINI, G. PENNA, R., 1996; INSEAN Internal Report
6. DUNCAN, J. H., 2001; Spilling Breakers *Ann. Rev. Fluid Mech.*, vol. 33.
7. DUNCAN, J. H., 1983; The breaking and non-breaking wave resistance of a two-dimensional hydrofoil, *J. Fluid Mech.*, vol. 126, pp. 507-520.
8. TENNEKES, H. LUMLEY, J. L., 1972; A first course in turbulence, Cambridge, MA, U.S.A.: MIT Press.
9. DONG R.R., KATZ J., HUANG T.T., 1997; On the structure of Bow Waves on a Ship Model, *J. Fluid Mech.*, vol. 346, pp. 77-115
10. ROTH G. I, MASCENIK D. T., KATZ J., 1999; Measurements of the flow structure and turbulence within a ship bow wave, *Physics of Fluids* n. 11, vol. 11
11. LARSSON L., BABA, E. 1996; Ship resistance and flow computations *Advances in Marine Hydrodynamics*, vol.5, Editor M. Ohkusu, CMP, Southampton, Boston.
12. TROIANI G., 2004; Free Surface Turbulence: an experimental study at low Reynolds numbers, PhD. thesis, Università "La Sapienza", Roma.
13. <http://www.chesapeakebay.net/info/ecoint3a.cfm>
14. BONMARIN P., 1989; Geometric properties of deep-water breaking waves, *J. Fluid Mech.*, vol. 209, pp.405-433

15. TULIN M.P., LANDRINI M., 2000; Breaking waves in the ocean and around ships, 23rd ONR Symposium on Naval Hydro., Val de Reuil (France).
16. TULIN M.P., 1996; Breaking of ocean waves and downshifting, Waves and Nonlinear Processes in Hydrodynamics, Grue J., Gjevik B., Weber J.E. eds., pp 177-190, Kluwer Acad. Press.
17. STERN F., LONGO J., PENNA R., OLIVIERI A., RATCLIFFE T., COLEMAN H., 2000; International collaboration on benchmark CFD validation data for surface combatant DTMB model 5415, 23rd ONR Symposium on Naval Hydro., Val de Reuil (France).
18. FU, T. C., KARION, A., RICE, R. J., WALKER, D. C., 2004; Experimental study of the bow wave of the R/V Athena I, 25th ONR Symposium on Naval Hydro, St. John's, Canada.
19. WILSON, R., CARRICA, P., HYMAN, M., and STERN F., 2004; A single-phase level set method with application to breaking waves and forward speed diffraction problem, 25th ONR Symposium on Naval Hydro, St. John's, Canada.
20. LONGO J., STERN F., 2002; Effects of drift angle on model ship flow, Experiments in Fluids, 32, 558-69.
21. PISTANI F., 2005; "Influence of large scale breaking waves in the near field of ships", Ph.D. Thesis, University of Rome *La Sapienza*, in preparation.

Table 1. Towing tanks dimensions, water quality and physical parameters; for salinity values see [13].

2 TOWING TANKS				
		IIHR towing tank	INSEAN basin n. 2	
Length (m)		100	220	
Width (m)		3.048	9	
Depth (m)		3.048	3.6	
3 WATER QUALITY and PHYSICAL QUANTITIES				
		IIHR	INSEAN	Full scale
Water Type	–	Tap water	Spring water	Sea water
Water Density	ρ (kg/m ³)	999	998.5	1030*
Kinematic Viscosity	ν (m ² /s)	1.12×10 ⁻⁶	1.09×10 ⁻⁶	1.17×10 ⁻⁶
Surface Tension	σ (N/m)	0.0734	0.0734	0.0734
Salinity	ppt	< 0.5	< 0.5	≈ 30
Gravity acceleration	g (m/s ²)	9.8031	9.8033	9.806*
Test Temperature	T (C)	15.6	16.6	-

* data taken from literature

Table 2. Geometrical data for 5512, 2340 and full-scale.

3.1.1 PARAMETERS		5512	2340	Full scale
Scale factor	λ	46.6	24.824	1
Length between perpendiculars	L_{pp} (m)	3.048	5.720	142.0
Beam	B (m)	0.406	0.760	18.9
Draft	T (m)	0.132	0.248	6.16
Displacement	Δ (tons)	0.083	0.550	8636.0
Displaced Volume	∇ (m ³)	0.083	0.550	8425.4
Wetted surface area	S_w (m ²)	1.358	4.786	2949.5
3.1.1.1 HULL COEFFICIENTS				
L_{pp}/B	7.530	$C_B = \nabla / (L_{pp}BT)$		0.506
B/T	3.091	$C_P = \nabla / (L_{pp}A_X)$		0.613
Entrance angle α (deg)	11.0	$C_X = A_X/BT$		0.825

Table 3. Test conditions for wave elevation and velocity measurements for 2340.

3.2 <u>TEST CONDITIONS</u>	
Towing Tank	INSEAN basin n. 2
Speed (m/s)	2.621
Trim° (fixed)	0.069
Sinkage (fixed)	0.0032
3.3 <u>Other Measured Quantities</u>	
Total Resistance (N)	80.64
C_{TM}	4.91E-03
C_F (ITTC 57)	2.84E-03
C_R ($k = 0$)	2.07E-03

Table 4. Uncertainty assessment results for the wave elevation: wave height (mean and *rms*) expressed in L_{PP} ; uncertainties are in percentage of the related dynamic ranges ($\langle h \rangle = -60.6 \div 103$ mm; $hrms_{max} = 11.3$ mm).

x	y	$\langle h \rangle$	$\langle hrms \rangle$	$U_{\langle h \rangle}$	U_{hrms}
0.100	-0.09	$3.91 \cdot 10^{-3}$	$5.81 \cdot 10^{-5}$	$B_{A/D} = 0.21\%$ $B_{KK} = 0.20\%$ $P = 0.26\%$ $U = 0.40\%$	$B_{A/D} = 3.1\%$ $B_{KK} = 0.20\%$ $P = 0.5\%$ $U = 3.1\%$
0.125	-0.09	$5.20 \cdot 10^{-3}$	$7.96 \cdot 10^{-5}$	$B_{A/D} = 0.21\%$ $B_{KK} = 0.20\%$ $P = 0.29\%$ $U = 0.41\%$	$B_{A/D} = 3.1\%$ $B_{KK} = 0.20\%$ $P = 0.70\%$ $U = 3.1\%$
0.150	-0.09	$9.07 \cdot 10^{-3}$	$8.53 \cdot 10^{-4}$	$B_{A/D} = 0.21\%$ $B_{KK} = 0.20\%$ $P = 0.56\%$ $U = 0.63\%$	$B_{A/D} = 3.1\%$ $B_{KK} = 0.20\%$ $P = 1.0\%$ $U = 3.2\%$

Table 5. Uncertainty assessment results for the three velocity components at the measuring point ($x = 0.20$, $y = -0.1015$, $z = -0.005$); $U^* = 2.621$ m/s for the axial velocity component, while, for transverse and vertical components U^* corresponds to their range of variation in the measured field.

	$\langle u \rangle$	$\langle v \rangle$	$\langle w \rangle$
Velocity	2.45 m/s $0.94 U_0$	-0.33 m/s $-0.12 U_0$	0.06 m/s $0.02 U_0$
Uncertainty	$B = 1.99 \cdot 10^{-2}$ m/s $P = 8.04 \cdot 10^{-3}$ m/s $Unc. = 2.15 \cdot 10^{-2}$ m/s $Unc./U^* = 0.82 \%$	$B = 9.62 \cdot 10^{-3}$ m/s $P = 2.59 \cdot 10^{-3}$ m/s $Unc. = 9.96 \cdot 10^{-3}$ m/s $Unc./U^* = 1.63 \%$	$B = 9.52 \cdot 10^{-3}$ m/s $P = 9.38 \cdot 10^{-4}$ m/s $Unc. = 9.56 \cdot 10^{-3}$ m/s $Unc./U^* = 1.56 \%$

Table 6. Non-dimensional parameters for 5512, 2340 and full scale.

Fr	U_{5512} (m/s)	U_{2340} (m/s)	$U_{full\ scale}$ (m/s)	$U_{full\ scale}$ knots	We_{5512}	We_{2340}	$We_{full\ scale}$	Re_{5512}	Re_{2340}	$Re_{full\ scale}$
0.28	1.531	2.097	10.450	20	312	585	14800	4.17×10^6	1.10×10^7	1.27×10^9
0.3	1.640	2.246	11.197	22	334	627	15800	4.46×10^6	1.18×10^7	1.36×10^9
0.325	1.777	2.434	12.130	24	362	679	17100	4.83×10^6	1.27×10^7	1.47×10^9
0.35	1.913	2.621	13.063	25	390	731	18400	5.21×10^6	1.37×10^7	1.59×10^9
0.375	2.050	2.808	13.996	27	418	783	19800	5.58×10^6	1.47×10^7	1.70×10^9
0.41	2.241	3.070	15.303	30	456	856	21600	6.10×10^6	1.61×10^7	1.86×10^9
0.45	2.460	3.370	16.795	33	501	940	23700	6.69×10^6	1.76×10^7	2.04×10^9

Table 7. Physical quantities for 5512, 2340 and full scale.

	IIHR	INSEAN	full scale
g (m/s ²)	9.8031	9.8033	9.81
ρ (kg/m ³)	999	998.5	1030
ν (m ² /s)	1.12E-06	1.09E-06	1.17E-06
σ (N/m)	0.0734	0.0734	0.0734
salinity	< 0.5ppt	< 0.5ppt	≈ 30 ppt

Table 8. Diverging waves wavelength and related Weber numbers (We^*) for 5512, 2340 and full scale.

Fr	λ_{5512} (m)	λ_{2340} (m)	$\lambda_{full\ scale}$ (m)	We^*_{5512}	We^*_{2340}	$We^*_{full\ scale}$
0.280	0.19	0.36	8.83	78	146	3679
0.300	0.22	0.41	10.14	90	168	4223
0.325	0.26	0.48	11.90	105	197	4957
0.350	0.30	0.56	13.80	122	229	5749
0.375	0.34	0.64	15.84	140	263	6599
0.410	0.41	0.77	18.94	168	314	7888
0.450	0.50	0.93	22.81	202	378	9503



Fig. 1. INSEAN basin N.2: the carriage.



Fig. 2. IIHR towing tank

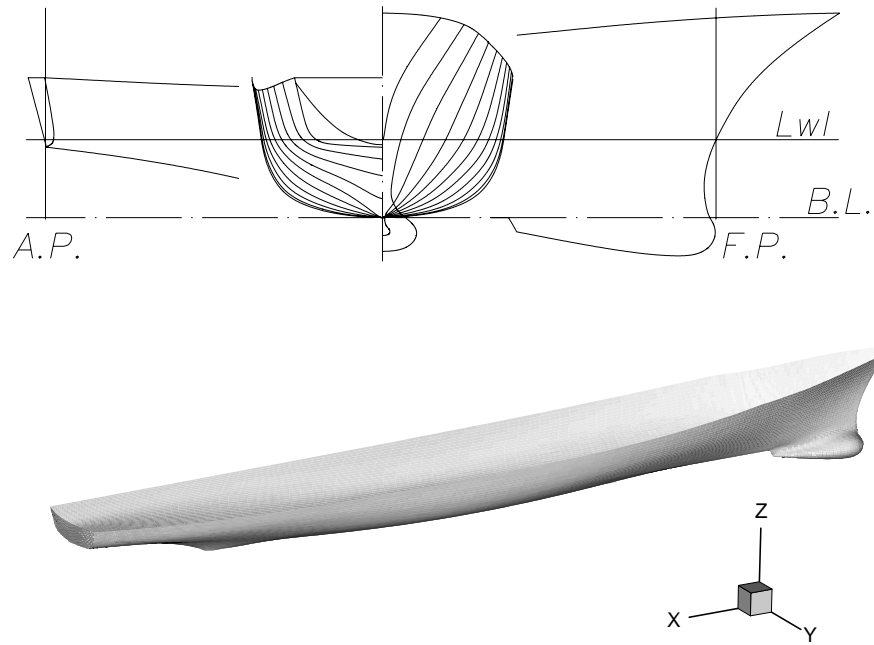


Fig. 3. Lines of the test models IIHR 5512 and INSEAN 2340 and reference frame.



Fig. 4. 2340 cut model

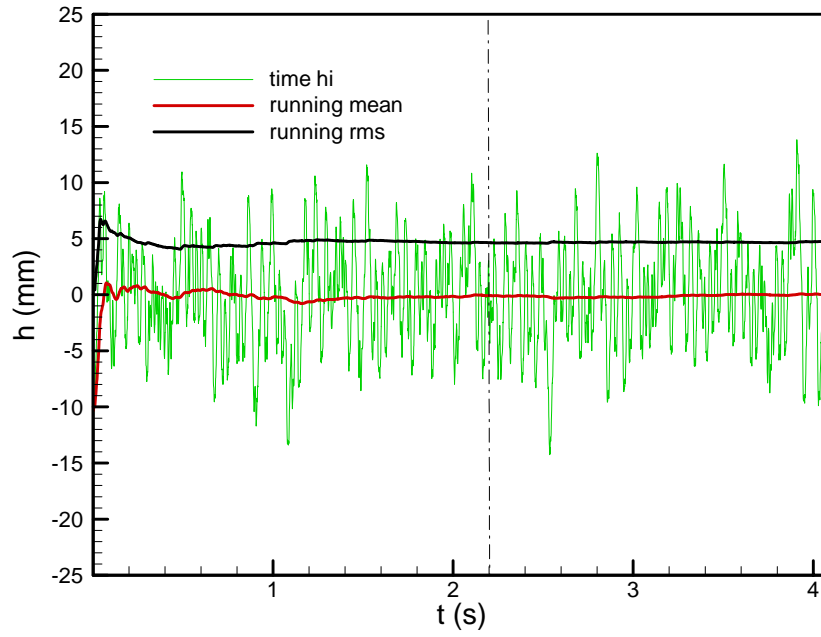


Fig. 5. Breaking wave height signal time history and running mean and rms ($x = 0.15$, $y = -0.09$); the asymptotic mean ($\langle h \rangle = 5.39$ mm) has been subtracted to the running mean in the figure. The dash dot line represents the chosen acquisition time for the wave height acquisitions.

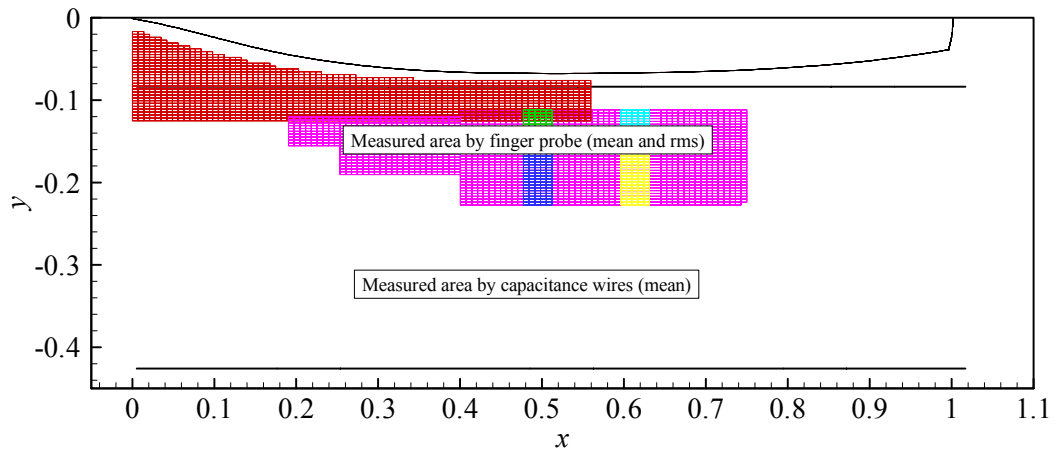


Fig. 6. Measured area by finger probe and capacitance wires.

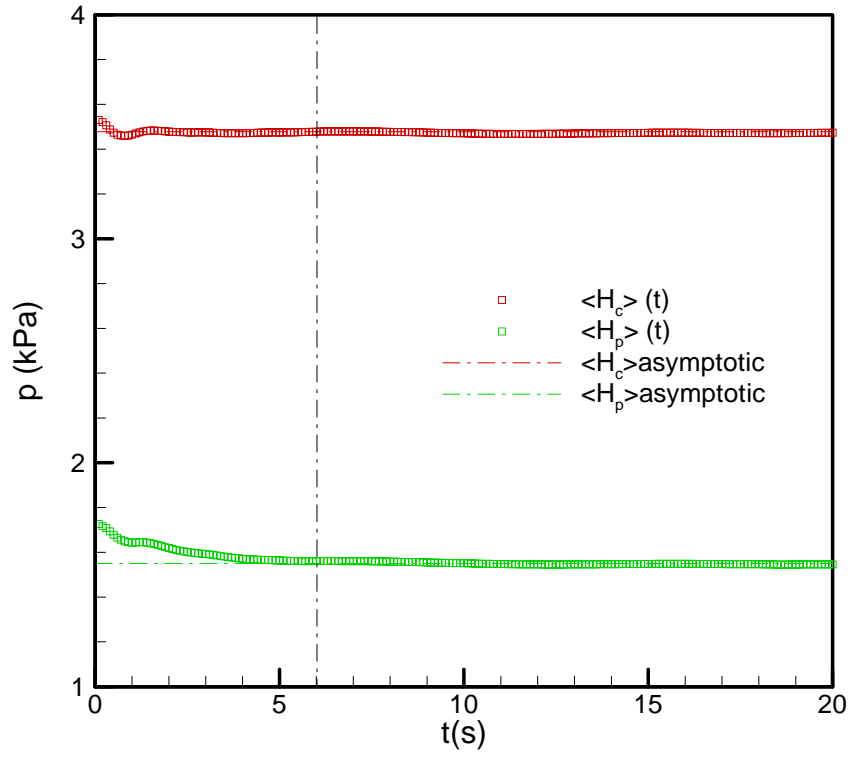


Fig. 7. Central and Port pressure ports running mean for a measurement point located under the breaking. The dash dot line represents the chosen acquisition time for the velocity acquisitions under the breaking.

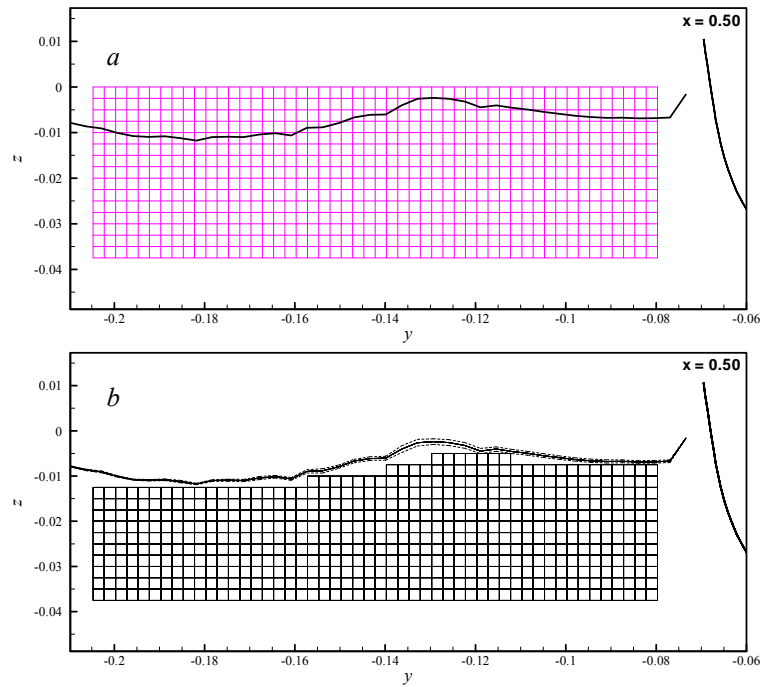


Fig. 8. Measurement grid at $x = 0.5$: a) designed grid; b) properly acquired points.

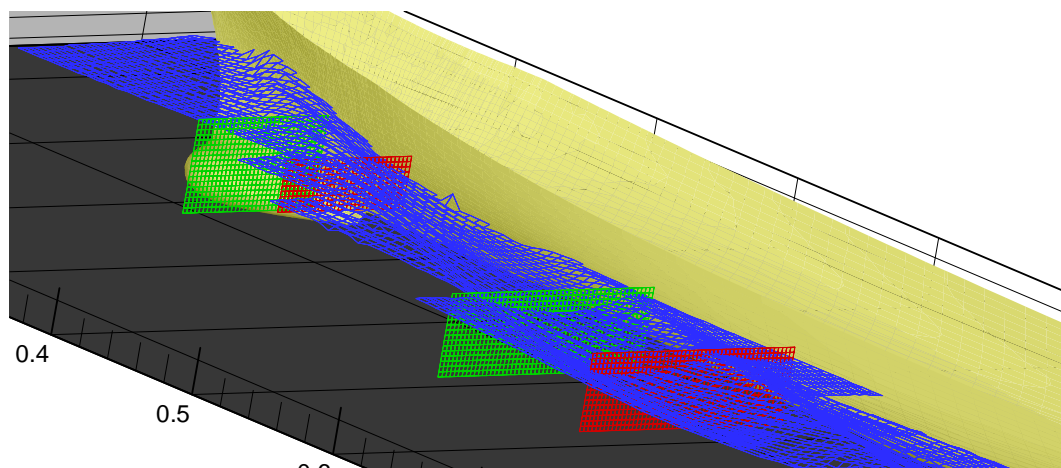


Fig. 9. Selected cross planes for the velocity measurements.

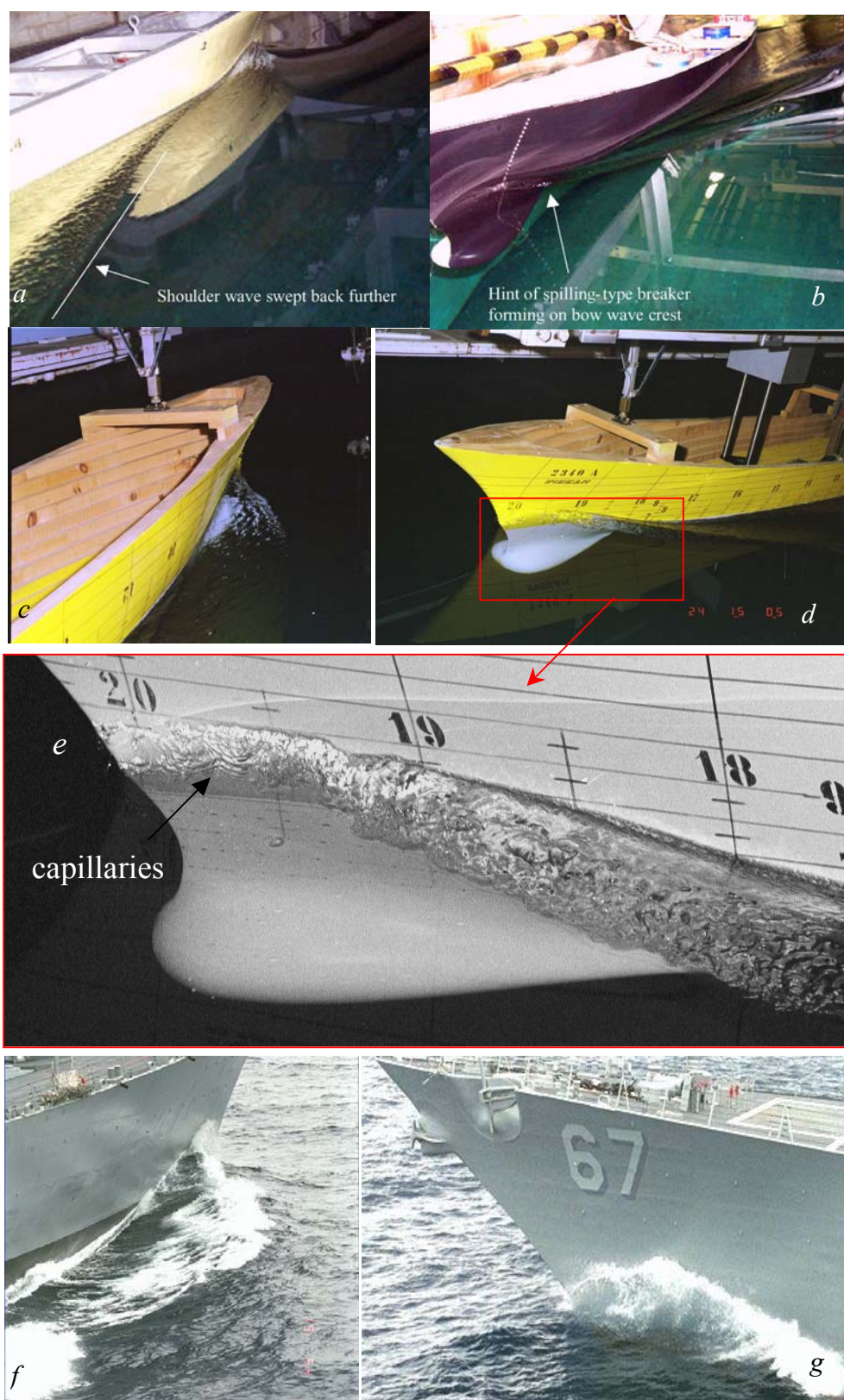


Fig. 10. $Fr=0.28$: 5512 side and front view (a, b); 2340 side and front view (c, d); evidence of capillaries for 2340 (e); full scale side and front view (f, g).

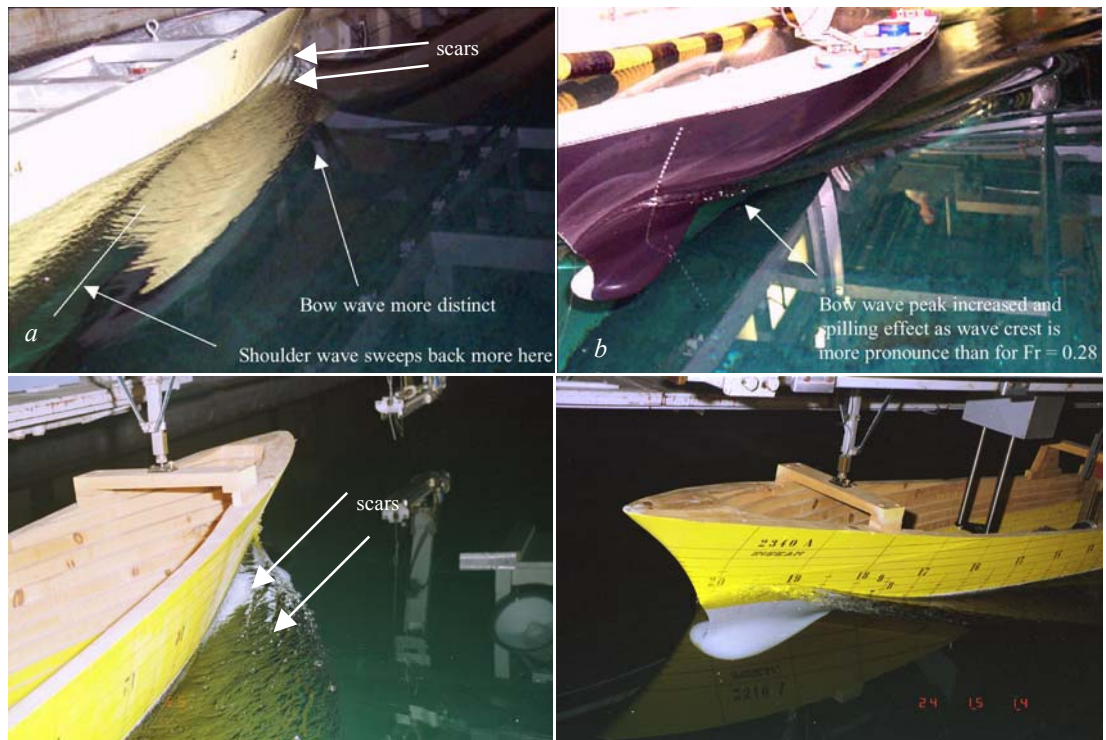


Fig. 11. $Fr=0.30$: 5512 side and front view (*a, b*); 2340 side and front view (*c, d*)

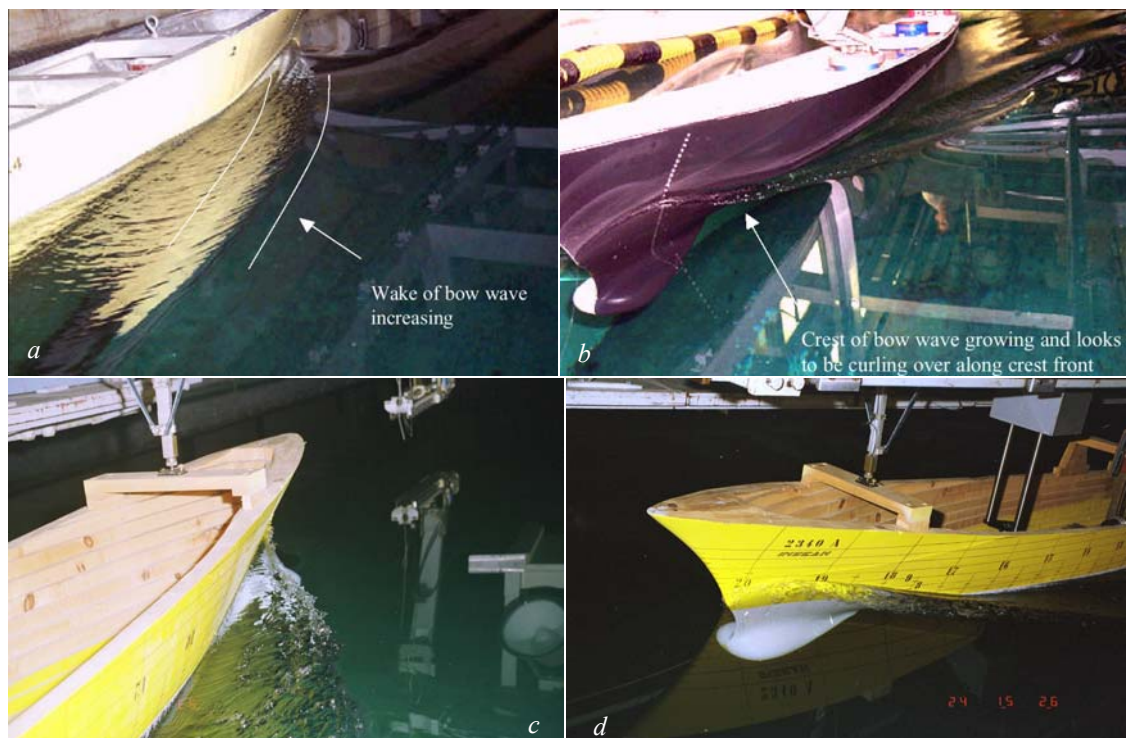


Fig. 12. $Fr=0.325$: 5512 side and front view (*a, b*); 2340 side and front view (*c, d*)

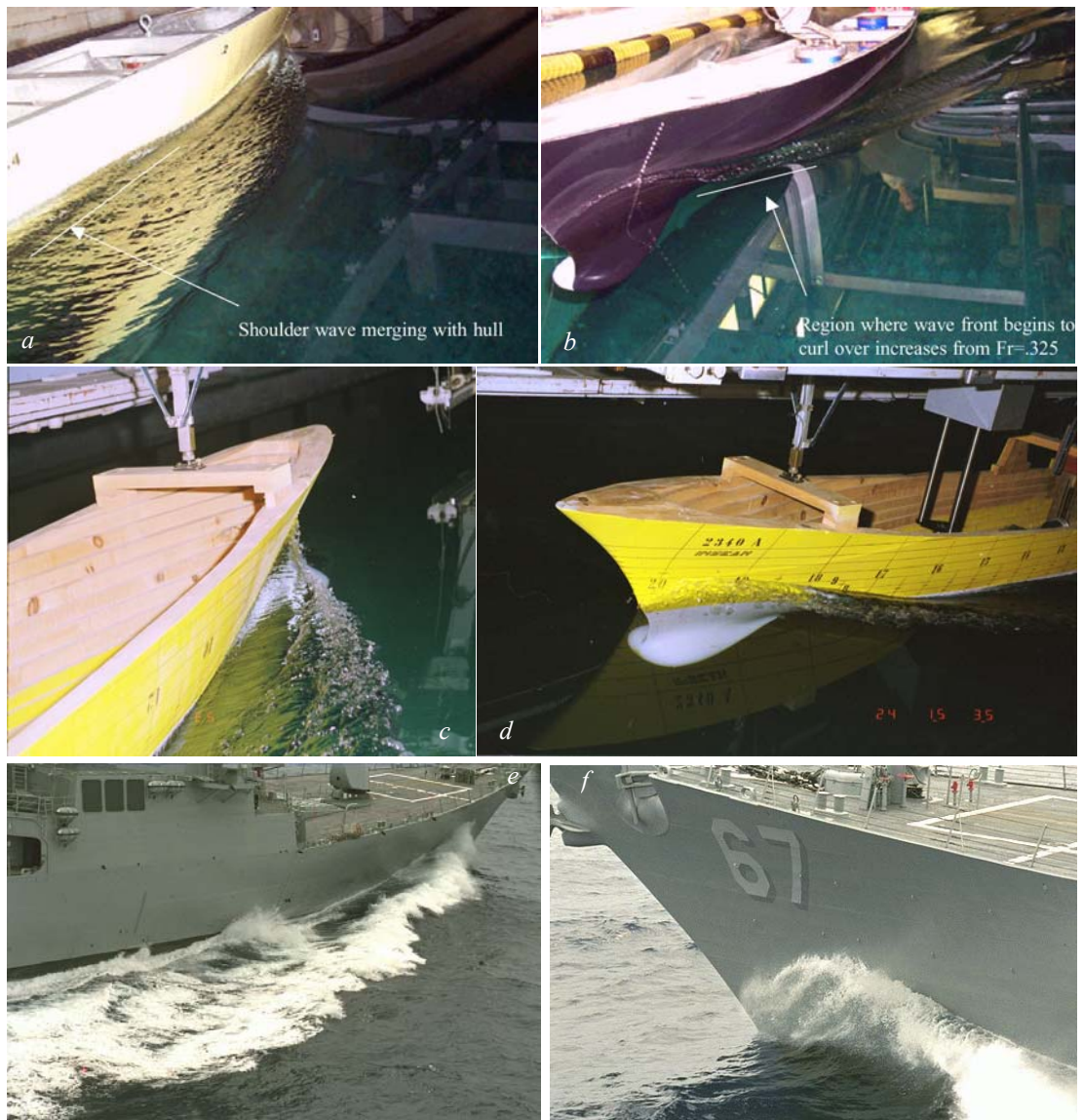


Fig. 13. $Fr=0.35$: 5512 side and front view (*a, b*); 2340 side and front view (*c, d*); full scale side and front view (*e, f*).

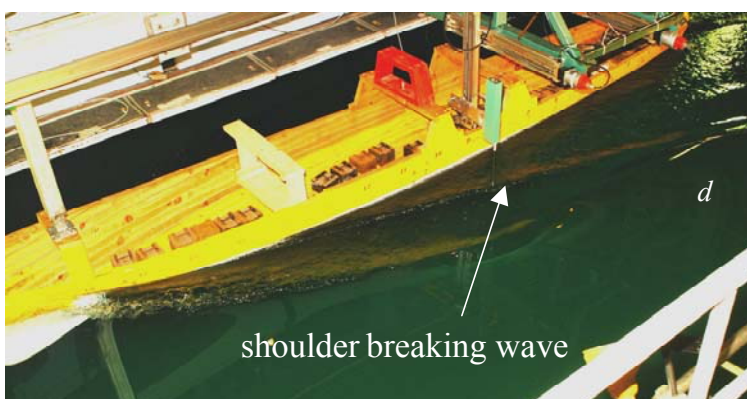
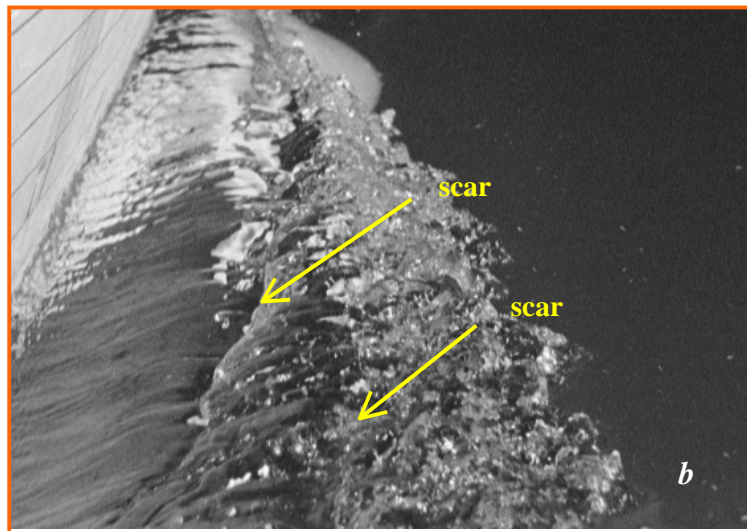
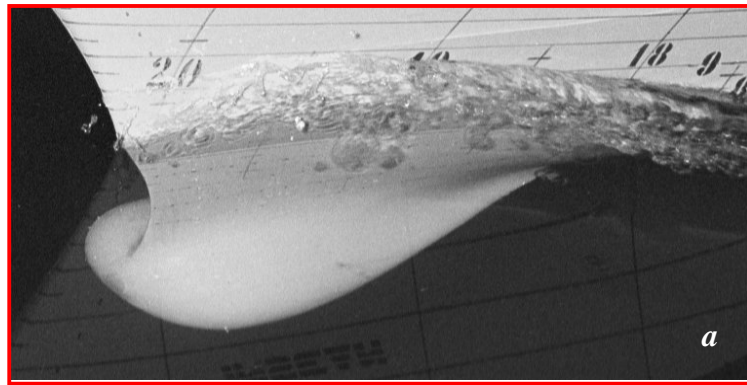


Fig. 14: $Fr=0.35$ rolls and scars generation and development (a, b, c); shoulder breaking wave(d).

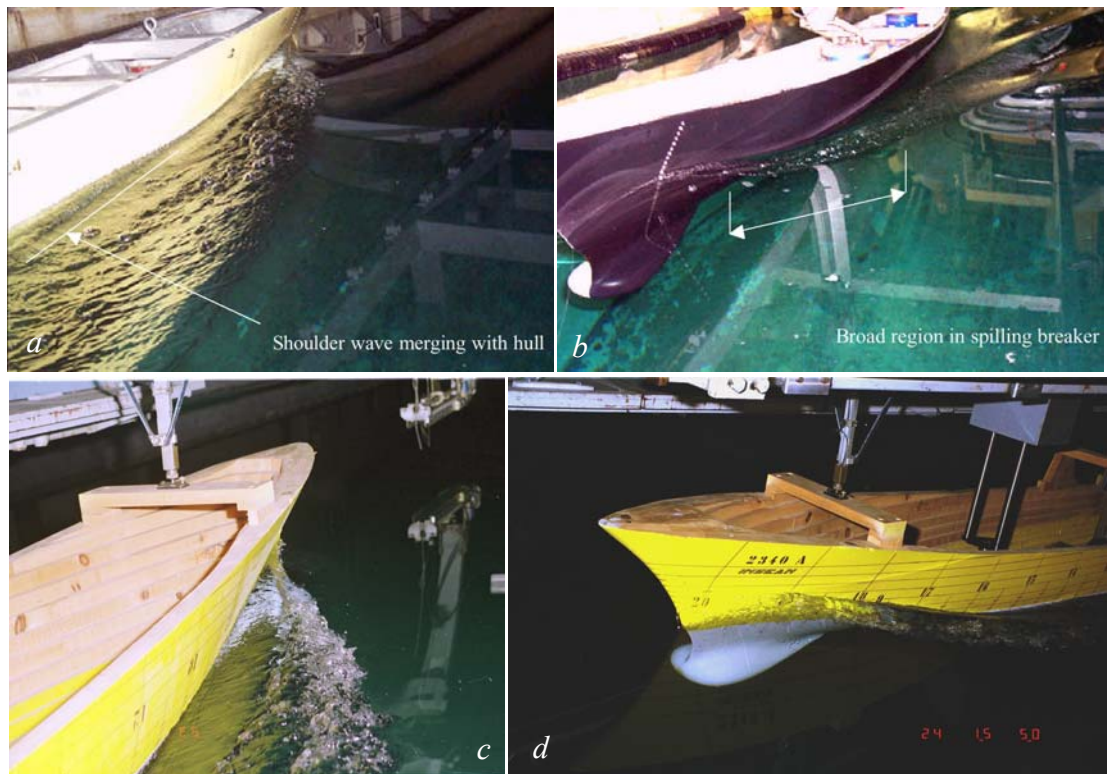


Fig. 15. $Fr=0.375$: 5512 side and front view (*a, b*); 2340 side and front view (*c, d*)

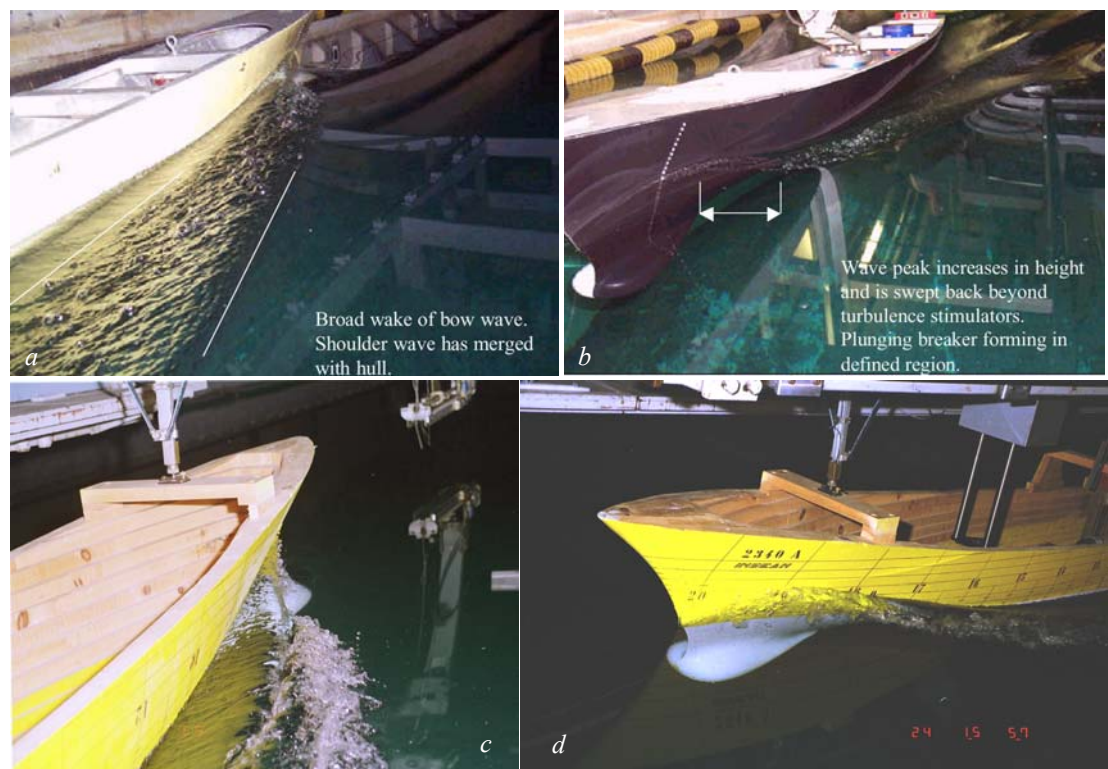


Fig. 16. $Fr=0.41$: 5512 side and front view (*a, b*); 2340 side and front view (*c, d*)

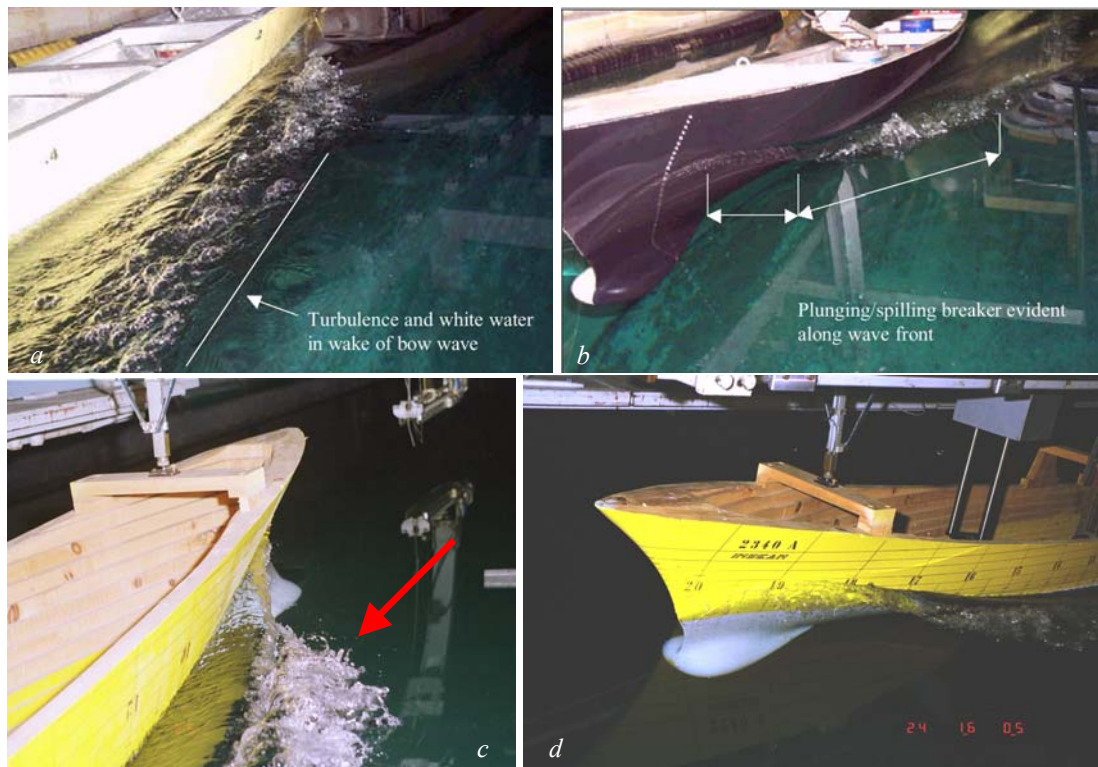


Fig. 17. $Fr=0.45$: 5512 side and front view (*a, b*); 2340 side and front view (*c, d*)

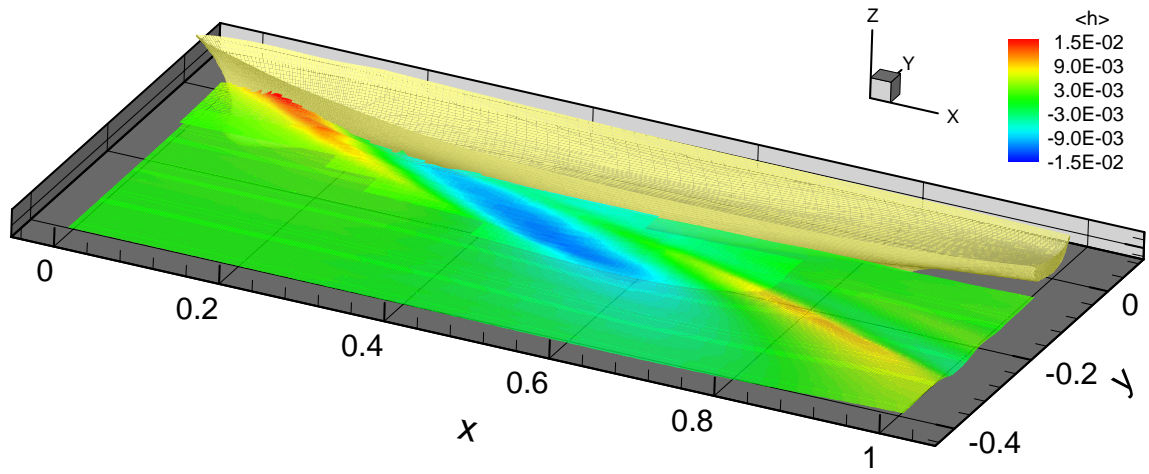


Fig. 18.a: Wave field (mean value).

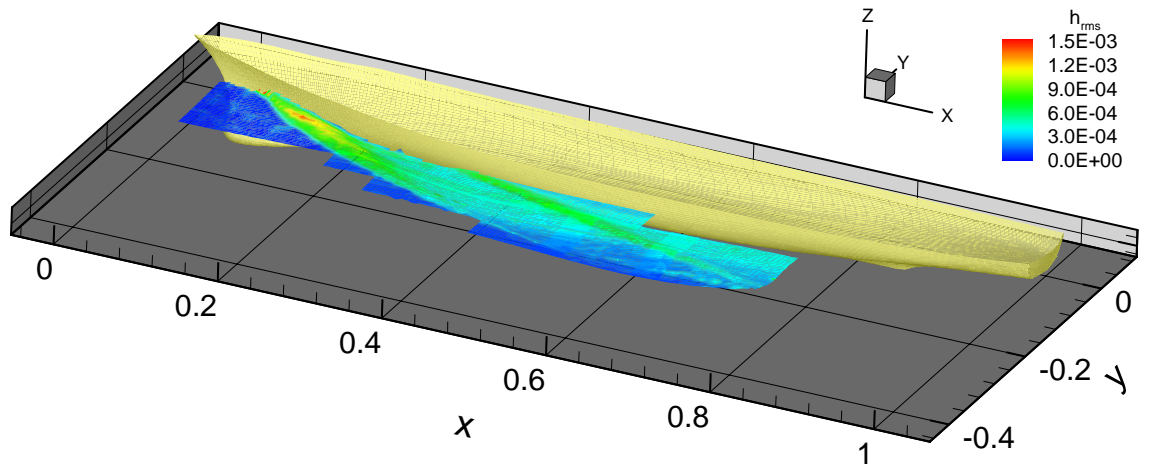


Fig. 18.b: Wave field (*rms* value).

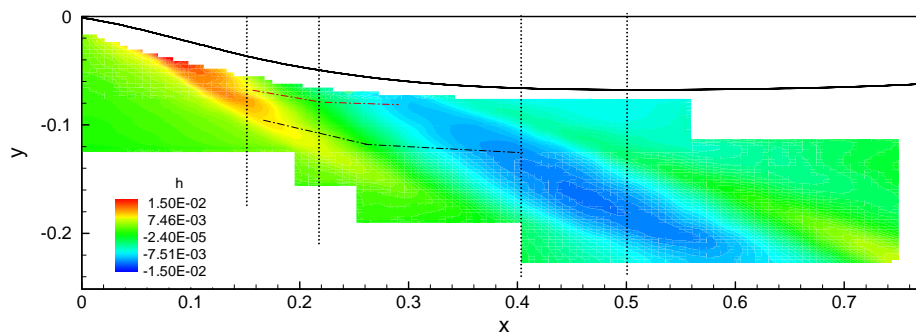


Fig. 19.a: Mean wave elevation measured by servo-mechanic probe; dash-dot lines indicated the scars locations; dotted lines indicated the sections where velocity measurements were carried out.

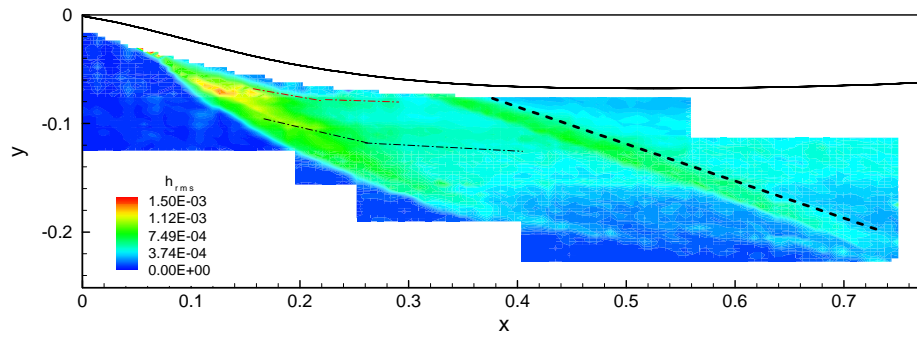


Fig. 19.b: rms value of the wave elevation measured by servo-mechanic probe; thin dash-dot lines indicate the scars locations and straight tick dash-dot line indicates the shoulder wave breaking.

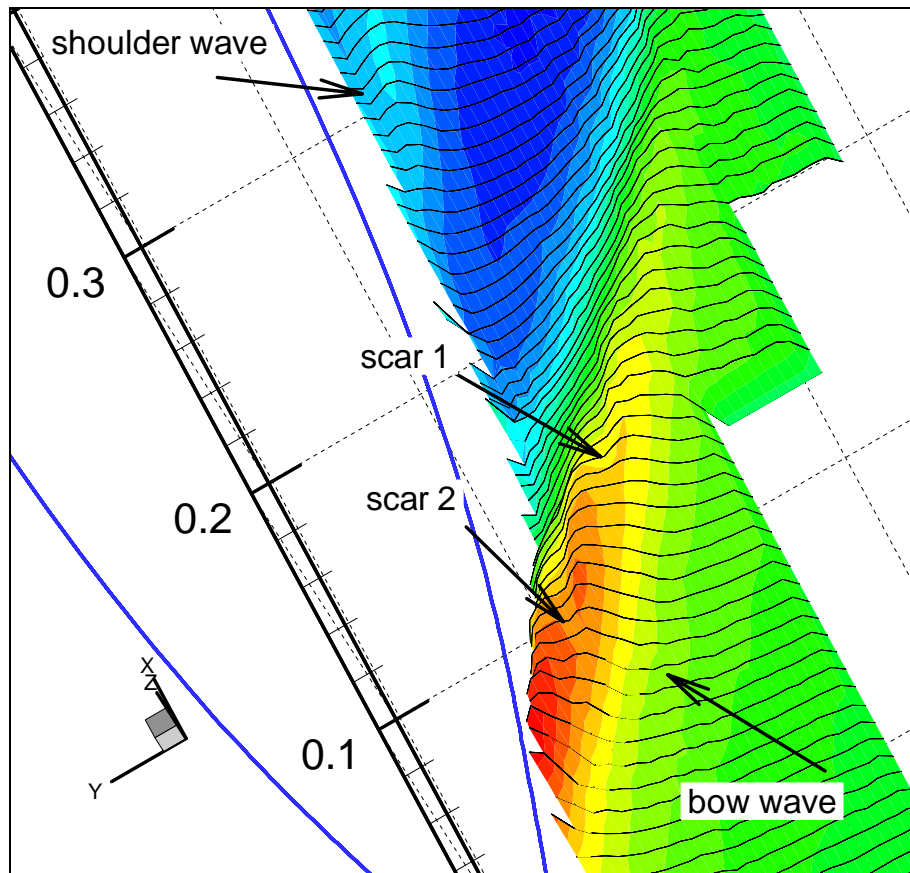


Fig. 20. a: traces of the scars generated at the bow; mean wave elevation

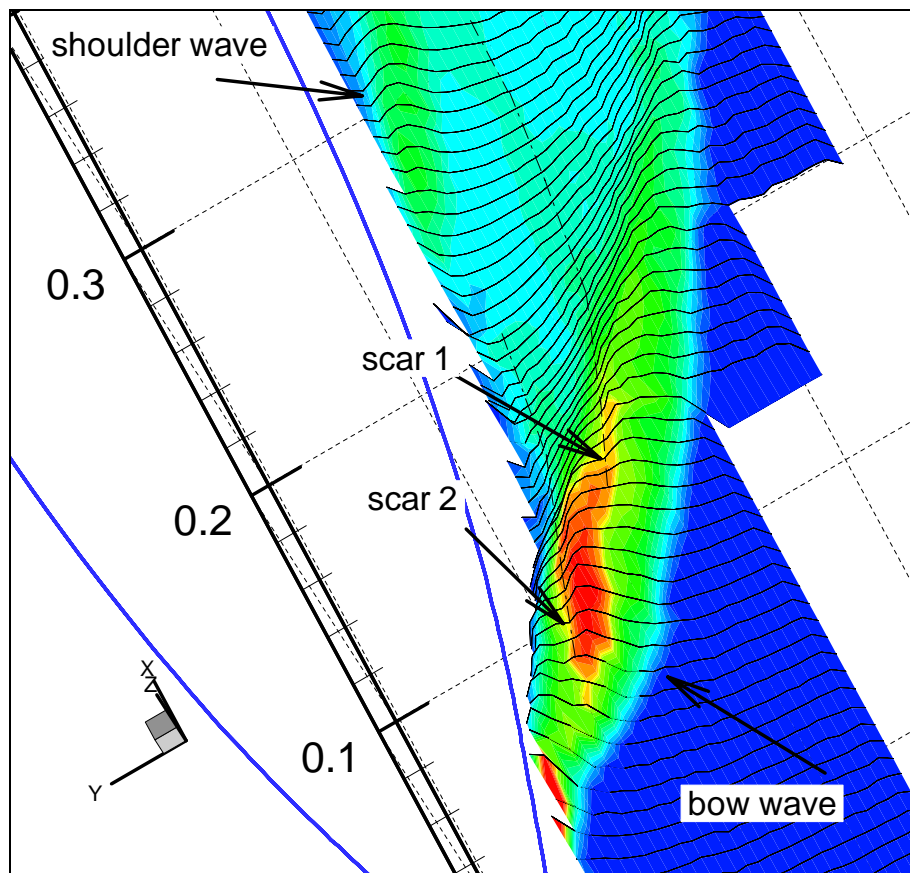


Fig. 20. b: traces of the scars generated at the bow; *rms* value of the wave elevation.

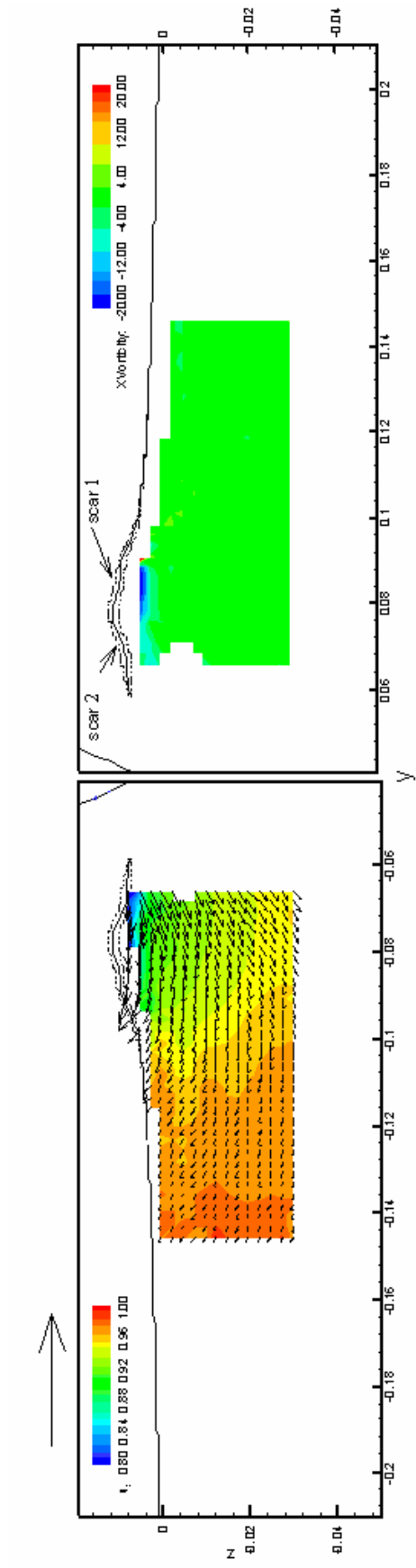


Fig. 21. $x = 0.15$: cross flow vectors and axial velocity contours (left); axial vorticity contours (right); arrow on top left represents the undisturbed velocity; data on the right side obtained mirroring data on the left side.

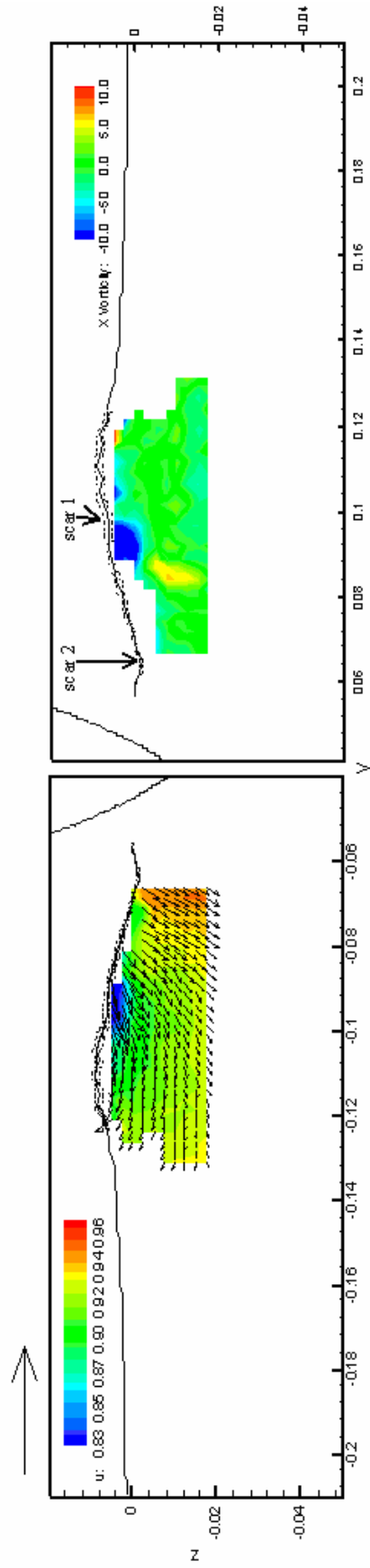


Fig. 22. $x = 0.20$: cross flow vectors and axial velocity contours (left); axial vorticity contours (right); arrow on top left represents the undisturbed velocity; data on the right side obtained mirroring data on the left side.

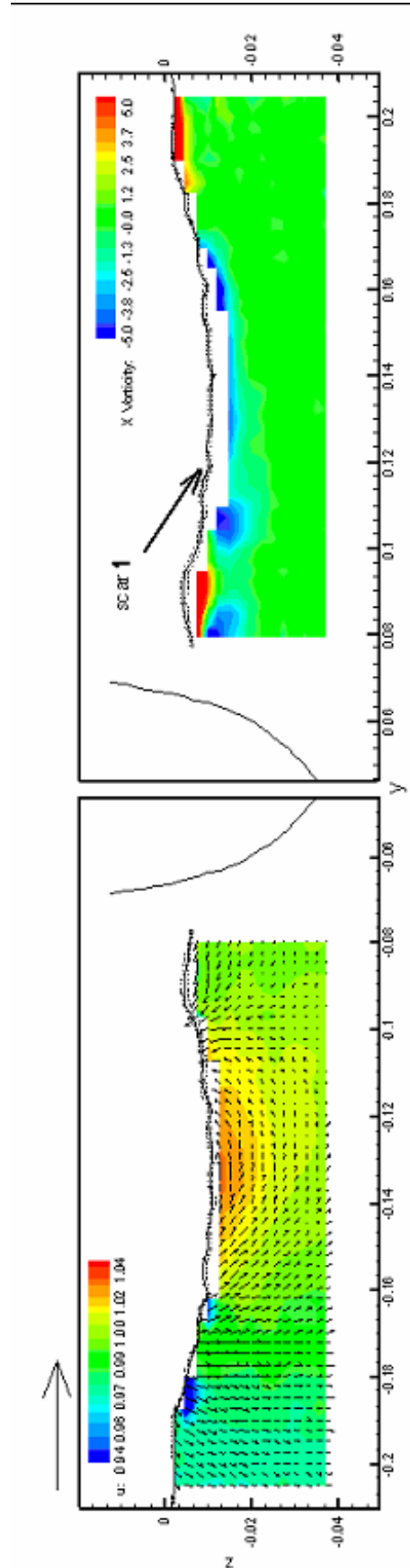


Fig. 23. $x = 0.40$: cross flow vectors and axial velocity contours (left); axial vorticity contours (right); arrow on top left represents the undisturbed velocity; data on the right side obtained mirroring data on the left side.

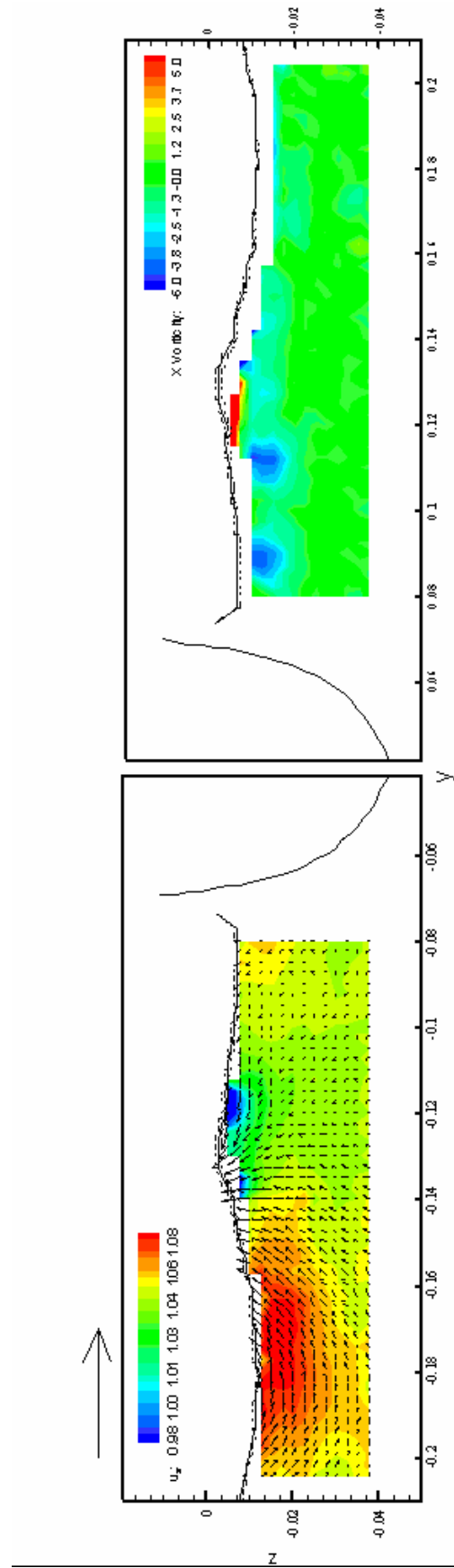


Fig. 24. $x = 0.50$: cross flow vectors and axial velocity contours (left); vorticity contours (right); arrow on top left represents the undisturbed velocity; data on the right side obtained mirroring data on the left side.

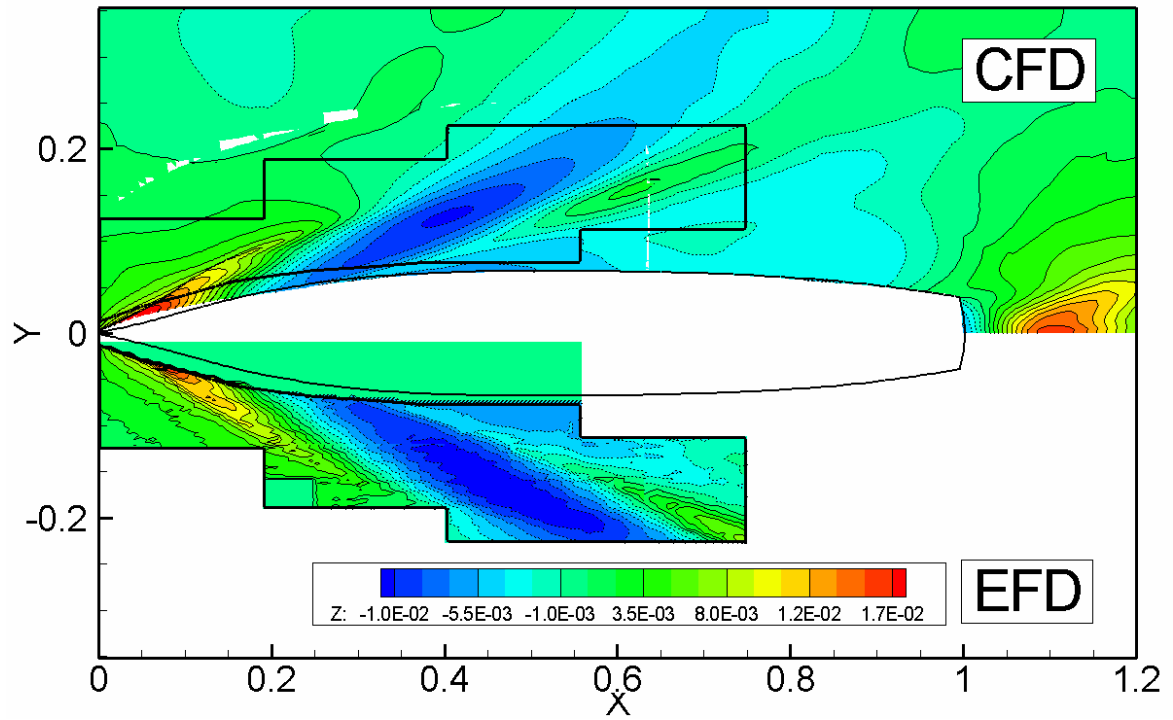


Fig. 25 Free surface contours for the surface combatant in calm water.

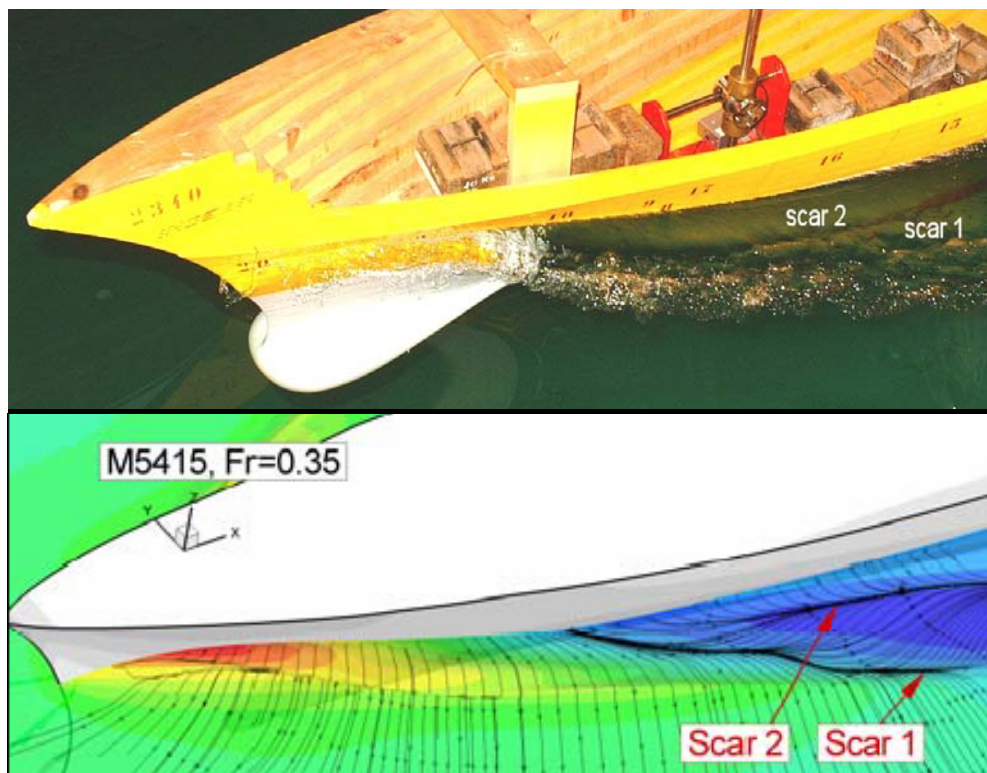


Fig. 26 scars and perturbation surface streamlines: picture taken during experiments (top); IIHR CFD [19] (bottom).

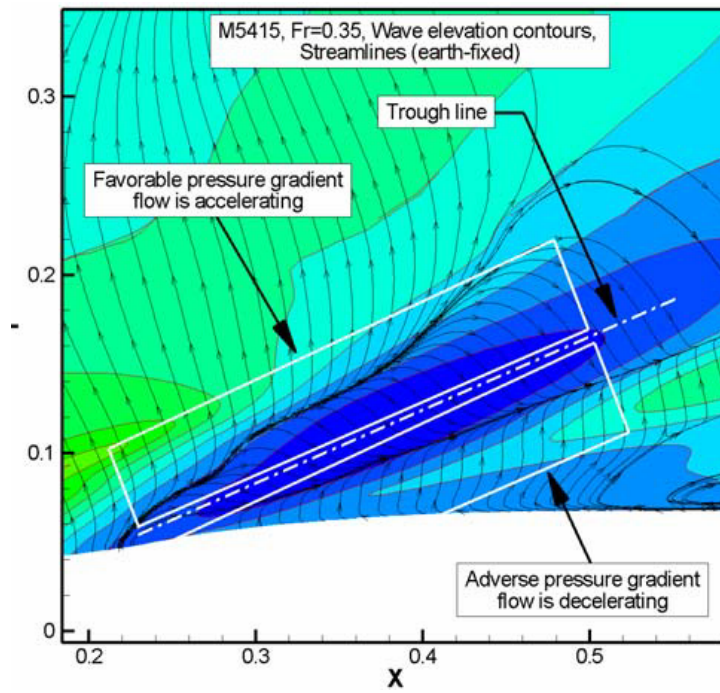


Fig. 27 Trough detail of free-surface contours and perturbation streamlines.

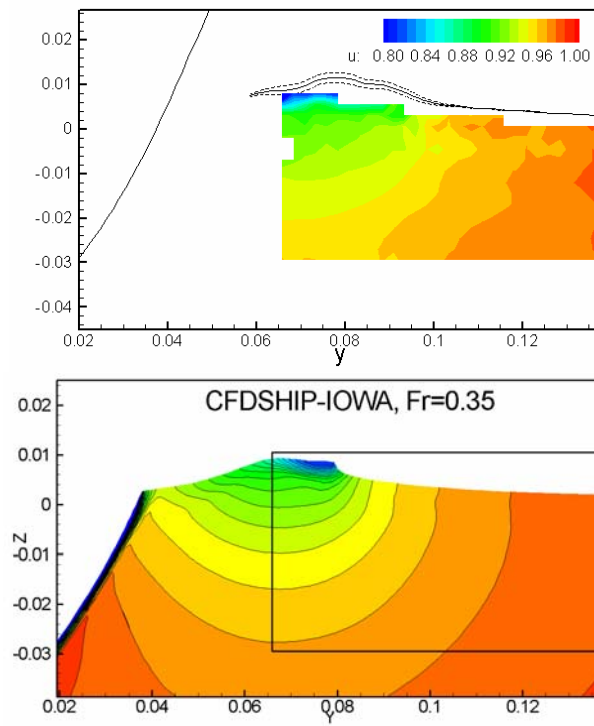


Fig. 28.a axial velocity pattern ($x = 0.15$): INSEAN experiments (left); IIHR CFD [19] (right).

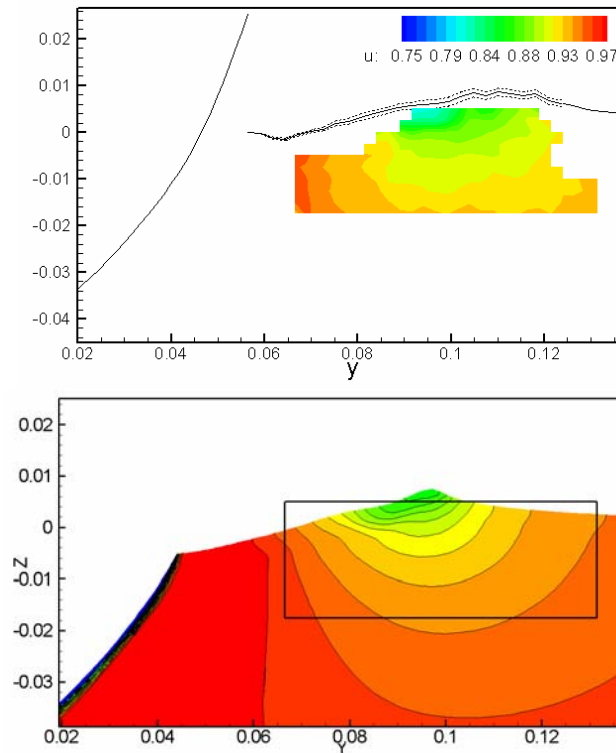


Fig. 28.b axial velocity pattern ($x = 0.20$): INSEAN experiments (left); IIHR CFD [19] (right).

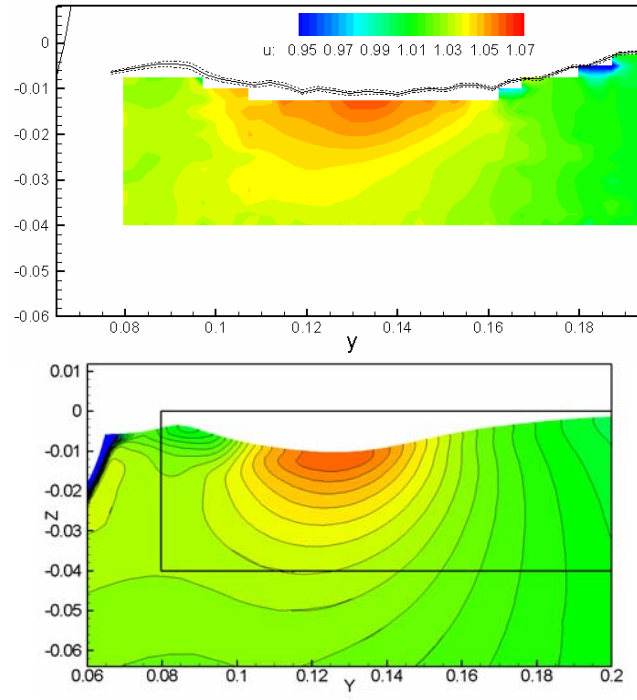


Fig. 28.c axial velocity pattern ($x = 0.40$): INSEAN experiments (left); IIHR CFD [19] (right).

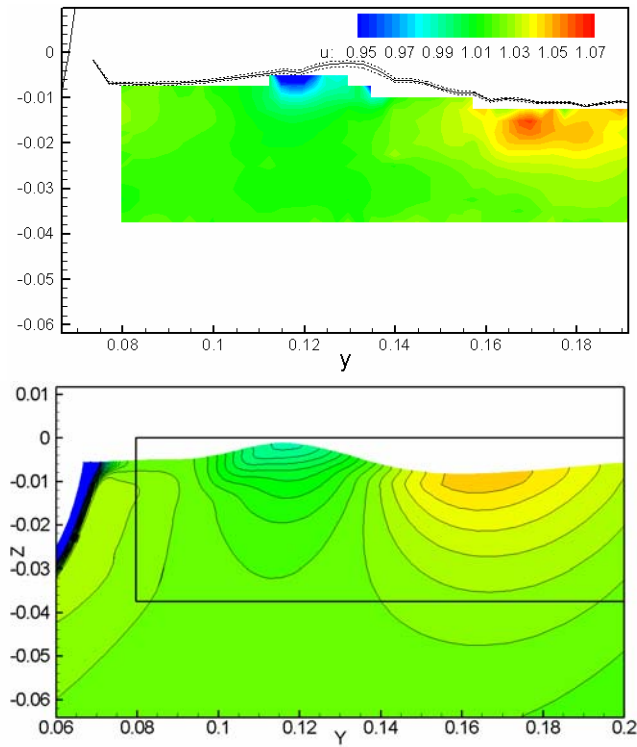


Fig. 28.d axial velocity pattern ($x = 0.50$): INSEAN experiments (left); IIHR CFD [19] (right).

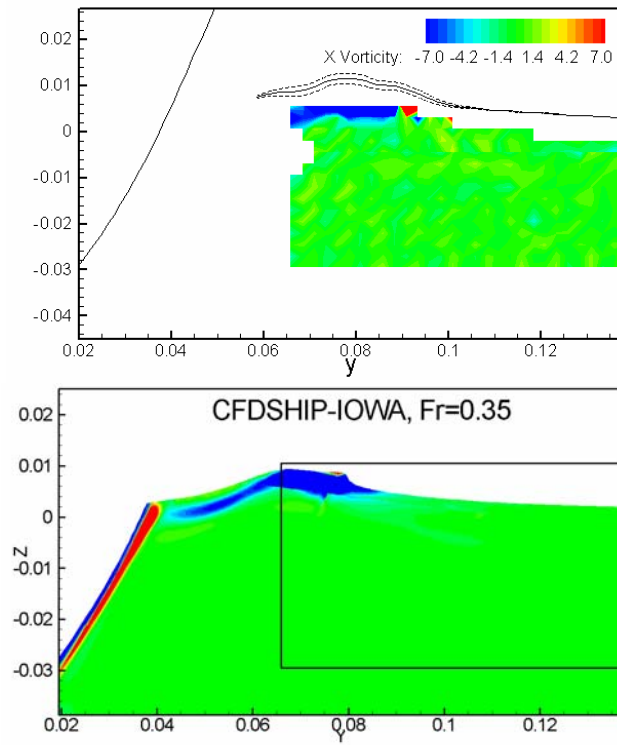


Fig. 29.a axial vorticity pattern ($x = 0.15$): INSEAN experiments (left); IIHR CFD [19] (right).

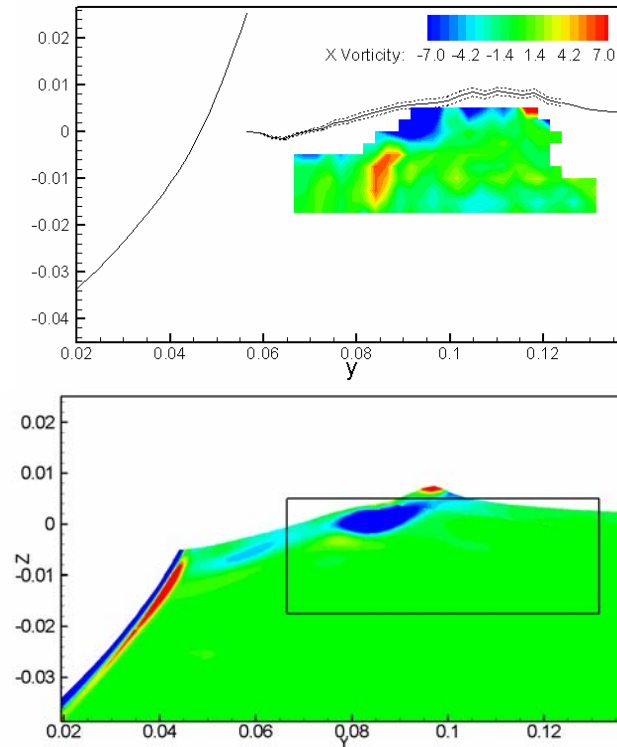


Fig. 29.b axial vorticity pattern ($x = 0.20$): INSEAN experiments (left); IIHR CFD [19] (right).

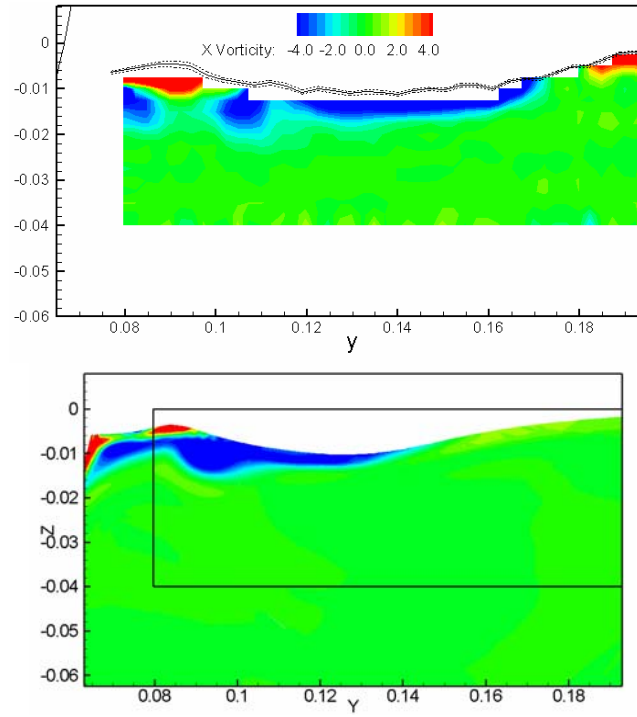


Fig. 29.c axial vorticity pattern ($x = 0.40$): INSEAN experiments (left); IIHR CFD [19] (right).

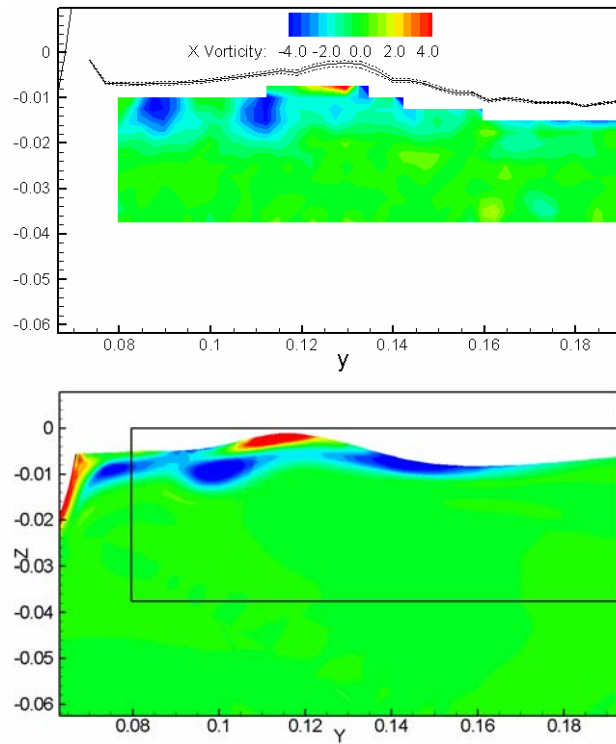


Fig. 29.d axial vorticity pattern ($x = 0.50$): INSEAN experiments (left); IIHR CFD [19] (right).

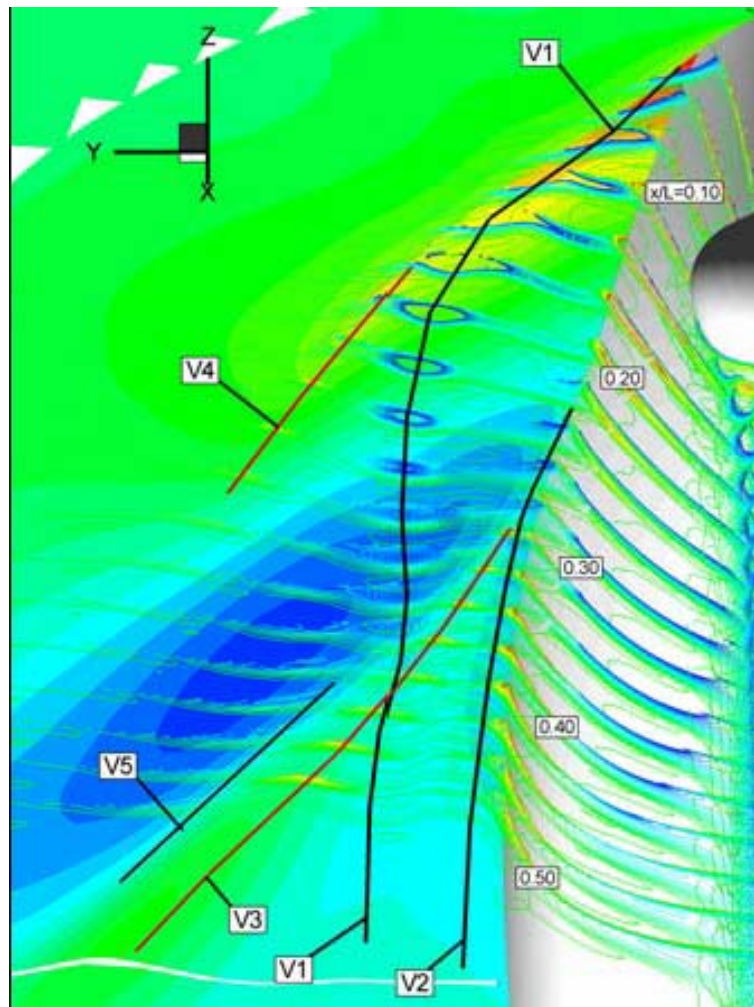


Fig. 30. Under free surface perspective of wave contours (background flood) and axial vorticity (slices)

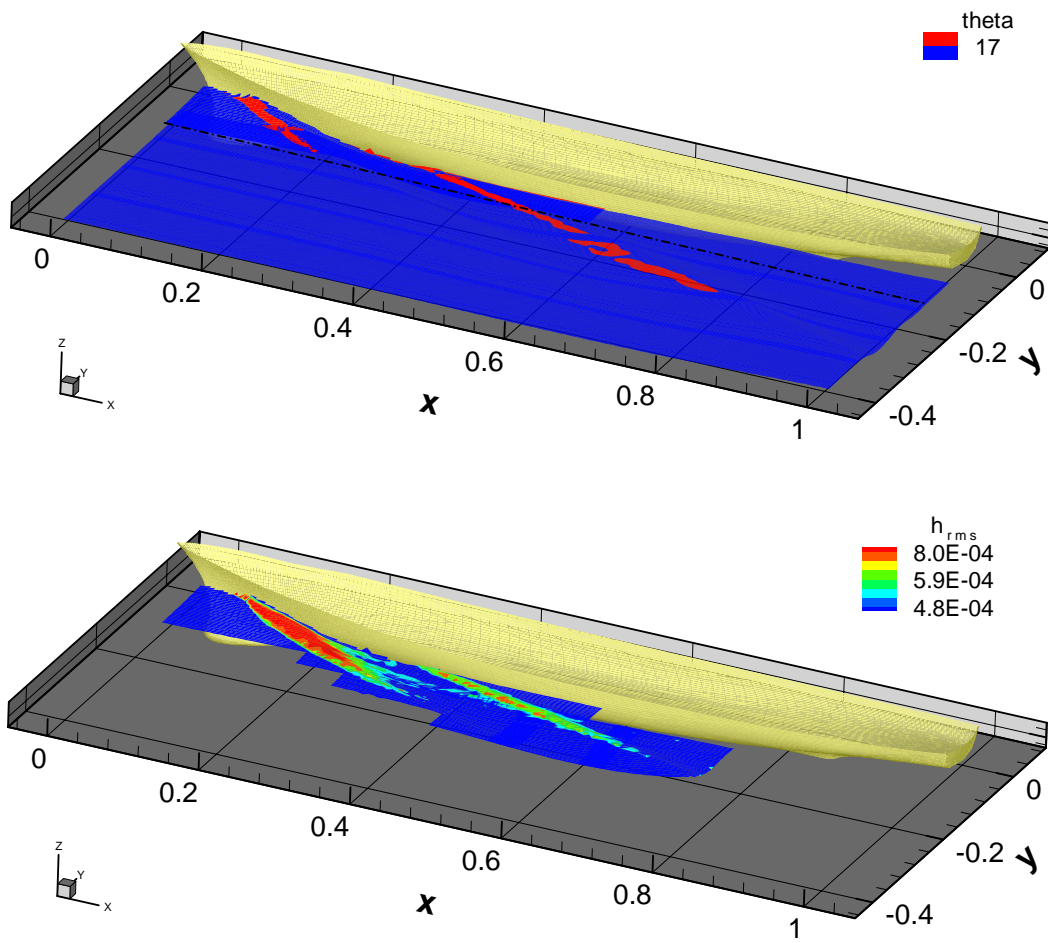


Fig. 31 wave steepness (top) and *rms* value of the wave elevation.